C: Physical Processes in Nanomaterials and Nanostructures

Probing Surface Effects on #-NaYF Nanoparticles by Nuclear Magnetic Resonance

Thiago B. de Queiroz, Michael Cabrera-Baez, Paulo Menegasso, Eduardo David Martínez, Ali Francisco García Flores, Carlos Rettori, and Ricardo Rodrigues Urbano

J. Phys. Chem. C, **Just Accepted Manuscript** • DOI: 10.1021/acs.jpcc.0c00776 • Publication Date (Web): 08 Apr 2020

Probing Surface Effects on α-$NaYF_4$ Nanoparticles by Nuclear Magnetic Resonance

Thiago B. de Queiroz,[*,†] Michael Cabrera-Baez,[*,‡] Paulo Menegasso,[¶] Eduardo D. Martinez,[§] Ali F. García Flores,[¶] Carlos Rettori,[*,†] and Ricardo R. Urbano[*,¶]

†*Centro de Ciências Naturais e Humanas, Universidade Federal do ABC, 09510-580, Santo André-SP, Brazil*

‡*Departamento de Física, Universidade Federal de Pernambuco, 50670-901, Recife-PE, Brazil*

¶*Instituto de Física "Gleb Wataghin", UNICAMP, Campinas, SP, 13083-859 Brazil*

§*Centro Atómico Bariloche, Comisión Nacional de Energía Atómica (CNEA), Consejo Nacional de Investigaciones Científicas y Técnicas (CONICET), Av. E. Bustillo 9500 R8402AGP San Carlos de Bariloche, Río Negro, Argentina*

E-mail: thiago.branquinho@ufabc.edu.br; mcabrera@df.ufpe.br; rettori@ifi.unicamp.br; urbano@ifi.unicamp.br

Abstract

The structural properties of insulating α-$NaYF_4$ (cubic) nanoparticles with size ranging within 4 - 25 nm were investigated by high-resolution ^{23}Na and ^{19}F solid-state Nuclear Magnetic Resonance (NMR) spectroscopy under magic angle spinning (MAS) with single pulse (SP-MAS), spin-echo (SE-MAS), inversion recovery, and 3Q-MAS experiments. The ^{23}Na SP-MAS spectra show a broad peak around -18 ppm with a shoulder around -9 ppm, which becomes more prominent for the smallest nanoparticles. The ^{23}Na nuclei resonating around -9 ppm demonstrate longitudinal relaxation time of few ms, while the ones resonating around -18 ppm are in the order of 50-125 ms. This feature is noticed for all studied nanoparticles, but it is more evident for the smallest ones ($\phi \lesssim 7$ nm), especially among the batches with higher polydispersity. Based on these relaxation times, field-dependent measurements and ^{23}Na 3Q-MAS, we attributed the signal around -18 ppm to ^{23}Na in the bulk of the nanoparticles and the signal around -9 ppm to surface or/and sites near defects, featuring higher fluctuations in the electric field gradient (EFG). The ^{23}Na 3Q-MAS spectra provide evidence for two (and sometimes three) distinct Na sites in α-$NaYF_4$ with similar quadrupole coupling but slightly different chemical shifts. The ^{19}F SE-MAS spectra show a broad peak around -75 ppm with a small shoulder around -120 ppm corresponding to only $\approx 1\%$ of the signal. The peak around -75 ppm is attributed to the stoichiometric $NaYF_4$ composition and its broadening is attributed to a distribution of Na and Y rich environments. The minor shoulder around -120 ppm is associated to the F deficient $NaYF_4$ structure. The ^{19}F spin-spin relaxation times indicates some degree of mobility of the fluorine atoms, possibly due to the presence of F-vacancies triggering hopping like ion motion. The signal related to the F deficient structure is greatly enhanced for the smallest nanoparticles (ϕ = 4 nm), i.e., along with the increase of ^{23}Na surface effects and defects. Therefore, we correlate several NMR techniques to provide fundamental structural view for nanoparticles used as upconversion host systems with prominent technological applications. Particularly for α-$NaYF_4$, significant surface effects and defects must be expected for nanoparticles with dimensions in the order of few nanometers ($\phi \lesssim 7$ nm).

1 Introduction

The design and development of nanocrystalline compounds are currently very attractive research topics due to their use in numerous technological applications.[1–3] An example is the Rare Earth (RE) doped $NaYF_4$ nanoparticles (NPs) that display interesting features arising from interactions between doping ions.[4,5] It makes these NPs suitable host materials in up-conversion processes, whereby incident infrared radiation is converted into visible light.[4,5] This nanocrystalline compound can be synthesized in two crystallographic phases,[6] cubic (α-phase) and hexagonal (β-phase). A recent study of the macro and microscopic properties of doped β-$NaYF_4$ nanoparticles revealed the important role of the electrostatic potential around the dopant ions in the optical properties, leading to a better comprehension of the up-conversion efficiency.[7] Despite these significant advances, many aspects of the structure of the nanoparticles are of current interest. For instance, there were significant disagreements concerning the structure of the β-$NaYF_4$ nanoparticles. Different space groups have been proposed to fit the X-ray diffraction (XRD) patterns observed for the bulk material[8] and NMR, as a technique sensitive to the local characteristics of the structure, was employed to finally conclude that it is formed as P63/m space group.[9]

Although the β-phase has been more extensively investigated because of its efficient up-conversion emission, the cubic α-$NaYF_4$ NP is postulated as the simplest structure to understand fundamental properties[10,11] such as surface effects in the structure. Previous NMR studies[12,13] investigated structural properties of undoped and Rare-Earth doped NPs, evaluating the quality of the crystals formed and the influence of the dopant in the crystalline lattice parameter and spin-diffusion. Despite the completeness of these studies, no size dependence on the structural properties influenced by surface effects was reported though they are among the fundamental features of nanoscaled materials. Focused on that issue we synthesized undoped α-phase $NaYF_4$ NPs with sizes ranging from 4 nm to 25 nm and characterized them by XRD, transmission electron microscopy (TEM), and ^{23}Na and ^{19}F

NMR. In particular, we associate spectral resolution with dissimilar relaxation times to probe subtle ^{23}Na site distortions and defects as a function of particle size and polydispersity.

2 Experimental details

2.1 Synthesis of the Nanoparticles

Pure cubic α-$NaYF_4$ NPs were synthesized by different methods to obtain a variety of particle sizes. For the smallest NP (named NP A) the co-precipitation method was performed following the process described by Wang et al.[14] and Liu et al.[15] Briefly, 4 mL of a 0.2 M $Y(CH_3COO)_3$ aqueous solution was added in a three-neck round bottom flask together with 7.2 mL of oleic acid (OA, technical grade, Sigma-Aldrich) and 16.8 mL of 1-octadecene (ODE, 90%, Sigma-Aldrich). Under magnetic stirring, the mixture was heated up to 120-140 ^{o}C to evaporate the water content and then cooled down to room temperature. At this point, a freshly prepared mixture containing 2 mL of a 1 M NaOH methanol solution and 8 mL of 0.4 M NH_4F solution in methanol was rapidly injected. The flask was heated to 50 ^{o}C for 30 minutes and then sealed. The temperature was raised to 100 ^{o}C and a vacuum pump was connected. After 15 minutes, the vacuum pump was turned off, a condenser was mounted, and the temperature was increased to 260 ^{o}C under an argon flux and maintained for 20 minutes. The flask was then removed from the mantle and allowed to cool down to room temperature. This method, typically used for the synthesis of small hexagonal-phase NPs, was performed at a lower temperature to delay the phase transformation from small cubic nuclei to larger hexagonal NPs.

For the syntheses of NPs of intermediate size (NP B, C, and D), thermal decomposition of trifluoroacetates was performed adapting the methods reported in Ref. 6. For NP B, 1 mmol of $Na(CF_3COO)$ (98%, Aldrich) and 1 mmol of $Y(CF_3COO)_3$ (99.99%, Aldrich) were added to 9.9 mL of oleylamine (OLA, technical grade, Sigma-Aldrich), 9.5 mL of OA and 19.2 mL of ODE in a three-neck round bottom flask. The mixture was heated up to

120-140 ^{o}C with vigorous magnetic stirring under vacuum for 30 minutes in a temperature-controlled electromantle to reduce the water and oxygen content. Then, under argon flux, the solution was heated up to a final temperature of 310 ^{o}C and maintained at this temperature for 30 minutes. The same procedure was performed for the synthesis of NP C. We report the characterization of NPs B and C, despite their analogous preparation, to observe how sensitive the batches are to uncontrolled preparation conditions (as ambient temperature, temperature fluctuations in the oven, and so on). For NP D, the final temperature was reduced to 300 ^{o}C and the reaction time extended up to 60 minutes. The lower temperature set in this case explains the smaller size obtained, as both nucleation and growth rates are strongly reduced at lower temperatures.

For the synthesis of the NP F, the largest NP in our study, a different procedure was performed, based on Ref. 16. First, a solution, labeled as solution X, was prepared in a round-bottom flask containing 2.5 mmol of $Na(CF_3COO)$, 2.5 mmol of $Y(CF_3COO)_3$, 5 mL of ODE and 10 mL of OA. Solution Y was prepared in a separate three-neck round-bottom flask containing a mixture of 10 mL of OA and 15 mL of ODE. Both solutions were heated up to 125 ^{o}C with vigorous magnetic stirring and kept at this temperature for 30 min under vacuum to remove residual water and oxygen. Afterwards, solution Y was heated up to 310 ^{o}C under argon flux and maintained at this temperature while solution X was transferred dropwise at a rate of 1 mL$\times$min^{-1} using a custom made syringe pump. After mixing the solutions, the temperature was lowered to 305 ^{o}C and maintained for 1 h under argon atmosphere. To obtain intermediate-size NPs (11 nm), NP E was prepared by the same procedure but the volumes of ODE and OA in solution Y were increased 1.5 times, as dilution affects the nucleation and growth process during the injection of solution X.

In all cases, after the reaction time was completed, the flask was removed from the mantle for cooling down to room temperature. An excess amount of ethanol was added and the NPs were extracted by centrifugation. A washing procedure was performed two times by dispersing the NPs in ethanol and centrifuging. An additional washing step to dissolve

and eliminate residual NaF was performed using a mixture of ethanol-water (50 v/v %).

2.2 XRD and TEM

The powder XRD measurements of the α-$NaYF_4$ NPs were carried out in a Bruker Phaser D2 diffractometer with Cu Kα radiation (λ = 1.5418 Å) using a silicon plate with zero background. Scan range was set from 20-60° with a step size of 0.02° and a count time of 5 s. TEM analyses were carried out using a JEOL JEM 2100F HRP (TEM-FEG) operating at 200 kV. For the analysis, the NPs were dispersed in toluene and dropped on a carbon film. Size counting statistics were measured semi-automatically using the ImageJ software.[17] For each batch, about 200 NPs where measured on the TEM images.

2.3 ^{19}F and ^{23}Na solid state NMR

^{23}Na SP-MAS, SE-MAS, inversion recovery, and 3Q-MAS experiments were conducted in a Varian VNMRS 500 MHz spectrometer, with magnetic flux density of 11.7 T, operating at the resonance frequency of 132.2 MHz with MAS of 15 kHz and at room temperature (25^o C). For the SP-MAS, a $\pi/2$ pulse length of 3.5 μs was employed using regular radiofrequency (rf) power such that nutation frequency was 71.4 kHz strength. The use of short excitation pulses corresponding to flip-angles smaller than 30^o resulted in identical spectra. For the SE-MAS and inversion recovery, low rf power were used in order to preferentially excite central transitions (CT) such that we obtained $\pi/2$ pulses of 12.5 μs with nutation frequency of 20 kHz strength (nutation experiments using such power resulted in regular sine functions). 3Q-MAS experiments were obtained by the three-pulse z-filtered sequence,[18–21] with a hard excitation of 5.3 μs and reconversion pulse of 1.8 μs (short pulses at nutation frequency of 100 kHz strength), and a detection pulse selective of the central transition of 15 μs (nutation frequency of 16.6 kHz strength), using a time increment τ_1 of 66.7 μs. ^{23}Na 3Q-MAS were not performed in NPs C and E since these time-demanding experiments would not provide any further information. Relaxation delays of 2 s were used in the SP-MAS, SE-MAS and

inversion recovery experiments, while 1 s was used in the 3Q-MAS. Chemical shifts are reported relative to Na^+ (NaCl 1M aqueous solution) at 0 ppm using solid NaCl as secondary reference at 7.21 ppm.[22] The NPs B and C present NaF as impurity in the ^{23}Na spectra even after ethanol washing, as well as in the XRD (for NP C), but this could be finally eliminated by washing out the samples with water. The ^{23}Na experiments were acquired accumulating from 64 until approximately 1600 scans, depending on the amount of sample available. The spectra were deconvoluted using the software DMFIT.[23] Additional ^{23}Na SP-MAS experiments were performed in Agilent DD2 and Bruker Avance Neo spectrometers at magnetic flux densities of 5.64 T and 14.1 T, with the ^{23}Na resonating at 64.1 and 158.8 MHz. All details on these experiments were similar to the ^{23}Na SP-MAS described above, except for the use of Agilent 1.6 mm and Bruker 1.3 mm probes. The use of such probes allowed us to perform experiments at variable MAS spinning frequencies, up to 35.7 kHz. The use of ^{19}F TPPM decoupling[24] in the ^{23}Na NMR experiments did not result in higher resolved spectra, independently of decoupling pulse power or phase-angle.

^{19}F MAS NMR spectra were measured in the same Agilent DD2 spectrometer with ^{19}F resonating at 228.04 MHz. The spectra were recorded in 1.6 mm rotors spinning at 35.7 kHz using a rotor-synchronized Spin-Echo sequence. The ^{19}F spectra were obtained after 2 rotor cycles for the echo formation (56 μs), which reproduces the SP-MAS spectra without significant background and baseline distortions. For spin-spin relaxation times (T_2) the SE-MAS was obtained after a range of 2-46 rotor cycles for the echo formation (i.e., with inter-pulse delay times, τ, ranging from 56 to 1288 μs). Relaxation delays of 160 s were used with $\pi/2$ pulses of 1.15 μs length (nutation frequency of 217.4 kHz strength). The relaxation delay was long enough to perform experiments after full relaxation in all samples, since the NPs with the larger sizes present relatively long ^{19}F T_1 (in particular, NP F shows $T_1 \approx 30$ s, as estimated from inversion recovery experiments). Up to 128 scans were accumulated and the chemical shifts are reported relative to $CFCl_3$ using solid NaF as a secondary reference at -224 ppm.[25]

3 Results and discussion

3.1 XRD and TEM characterization: Particle size and lattice parameter

Fig. 1 presents the XRD pattern for the α-$NaYF_4$ NPs (see Table 1 for size/label relation as obtained from XRD line broadening and TEM images counting). The peak positions correspond to the reported standard patterns of cubic α-$NaYF_4$ (JPCDS)[6] without any additional peak associated with impurities, except for the NP C that shows NaF impurities. In fact, ^{23}Na NMR demonstrates that the NPs B and C, as prepared, contain adsorbed NaF. This contaminant could be finally eliminated by washing out the samples with water (as commented in Sections 2.3 and 3.2). The lattice constants of all NPs were calculated to be 5.47(1) Å, in agreement with bulk α-$NaYF_4$. The broadening of the diffraction peaks is related to the small size of α-$NaYF_4$ nanoparticles. Using the Debye-Scherrer formula one obtains a group of smaller NPs with an average crystallite size of 4(1), 7(1), 7(1), and 6(1) nm for NPs A, B, C, and D, respectively, and a group of larger NPs, with sizes of 11(1) and 20(2) nm for NPs E and F, respectively.

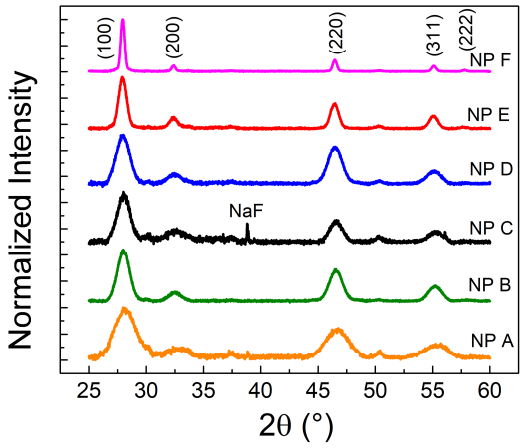

Figure 1: XRD pattern of NPs A-F, with peaks indexed according to the cubic structure of α-$NaYF_4$ (JCPDS card No. 77-2042).

Table 1: Size of the nanoparticles estimated by XRD and TEM images (diameters in nm).

Method*	NP A	NP B	NP C	NP D	NP E	NP F
XRD	4(1)	7(1)	7(1)	6(1)	11(1)	20(2)
TEM	4(1)	9(2)	12(9)	7(1)	11(7)	25(5)

*Note the difference in the deviations annotated in parenthesis: For the XRD, it is presented the standard deviation between experimental data and the Debye-Scherrer formula, while for the TEM it is presented the Full Width at Half Maximum (FWHM) of the Gaussian distribution fitted to the data (σ_{FWHM}).

Fig. 2 displays the room temperature TEM images of the NPs. Images in high resolution show lattice fringes (insets) indicating the crystalline nature of the NPs, clearly revealed by fast Fourier transform patterns. For all NPs the interplane distances match to those of the cubic structure, with 3.1 Å corresponding to d-spacing for the lattice plane (111) and 1.89 Å for the (220).

More detailed information about the particle size can be obtained from statistical analyses of the TEM images. Fig. 3 shows the particle size distributions for the NPs calculated from size-counting on more than 200 NPs taken from several images, with the histograms fitted to Gaussian distributions (see Table 1 for size parameters derived from the Gaussian fittings). NPs A, B, C, D, E, and F are characterized by particle size centered at 4(1), 9(2), 12(9), 7(1), 11(7), and 25(5) nm, respectively. The size dispersions are indicated in parenthesis, and were defined as the FWHM of the Gaussian distribution. The NPs A, D, and F present relatively narrow particle size distribution, around 20% of their particle size. The NPs B, C, and E present broader particle size distribution. For instance, NP B presents high counts ($\approx$ 20%) for particles ranging from 7 to 11 nm, while for NP C this range is from 10 to 17 nm. This results from small variations in the temperature during the preparation of the NPs, demonstrating that the formation of the NPs is highly sensitive to this parameter.[6,15]

The first finding from the comparison between XRD and TEM data is that for particles with higher polydispersity (NPs B and C) the Debye-Scherrer model has limited accuracy. The XRD peaks are not only broadened by a reduction in particle size but also due to polydispersity, defects and possibly local distortions from the cubic phase.[26] In the following,

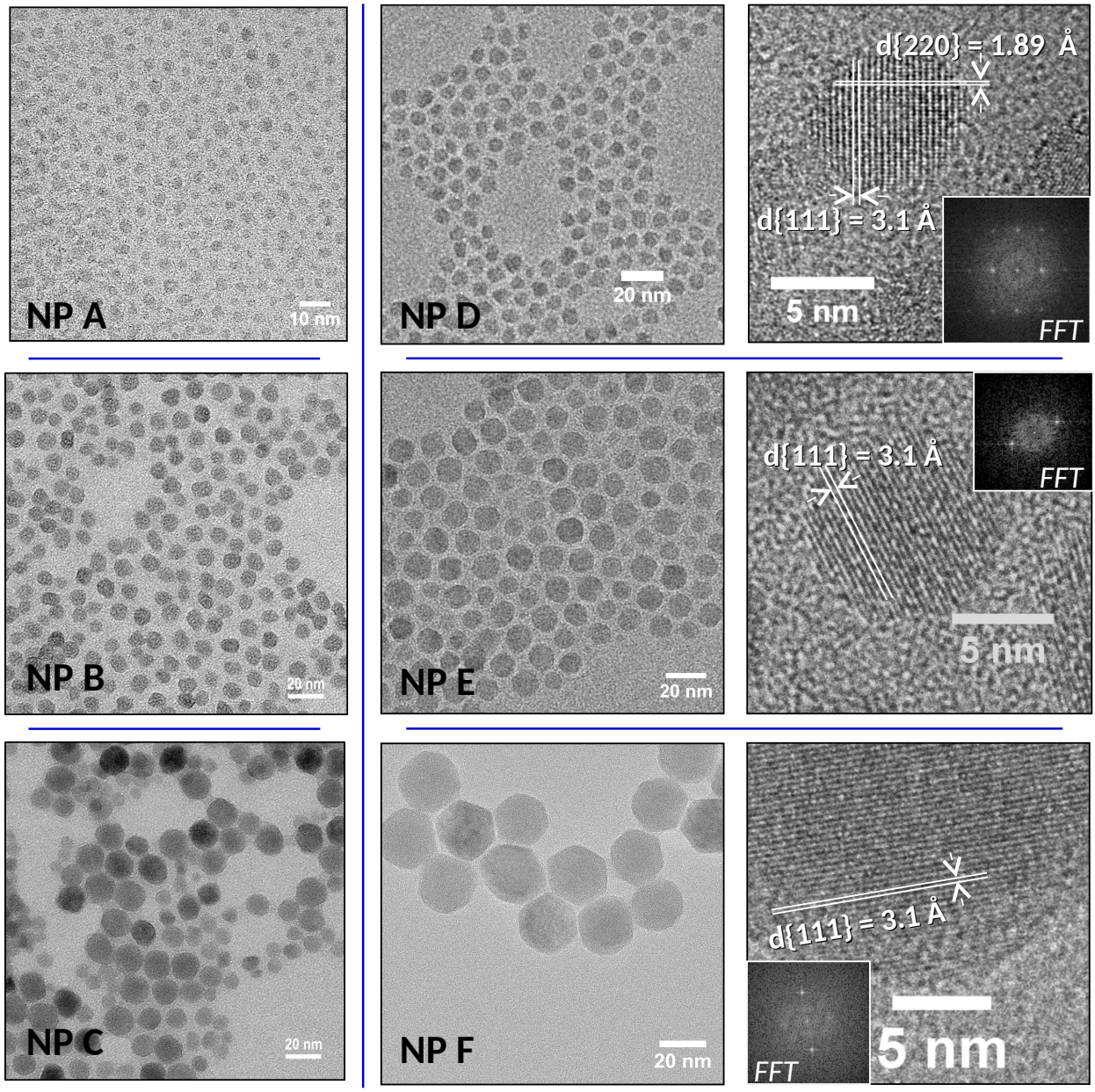

Figure 2: TEM images of the α-$NaYF_4$ NPs at low magnification (first and second rows) and selected high-magnification TEM images (third column) with lattice fringes as insets for NPs D, E, and F.

we discuss the surface effects and the presence of sites nearby defects as influenced by two parameters: particle size (contrasting NPs A, D, and F) and particle size distribution (or polydispersity).

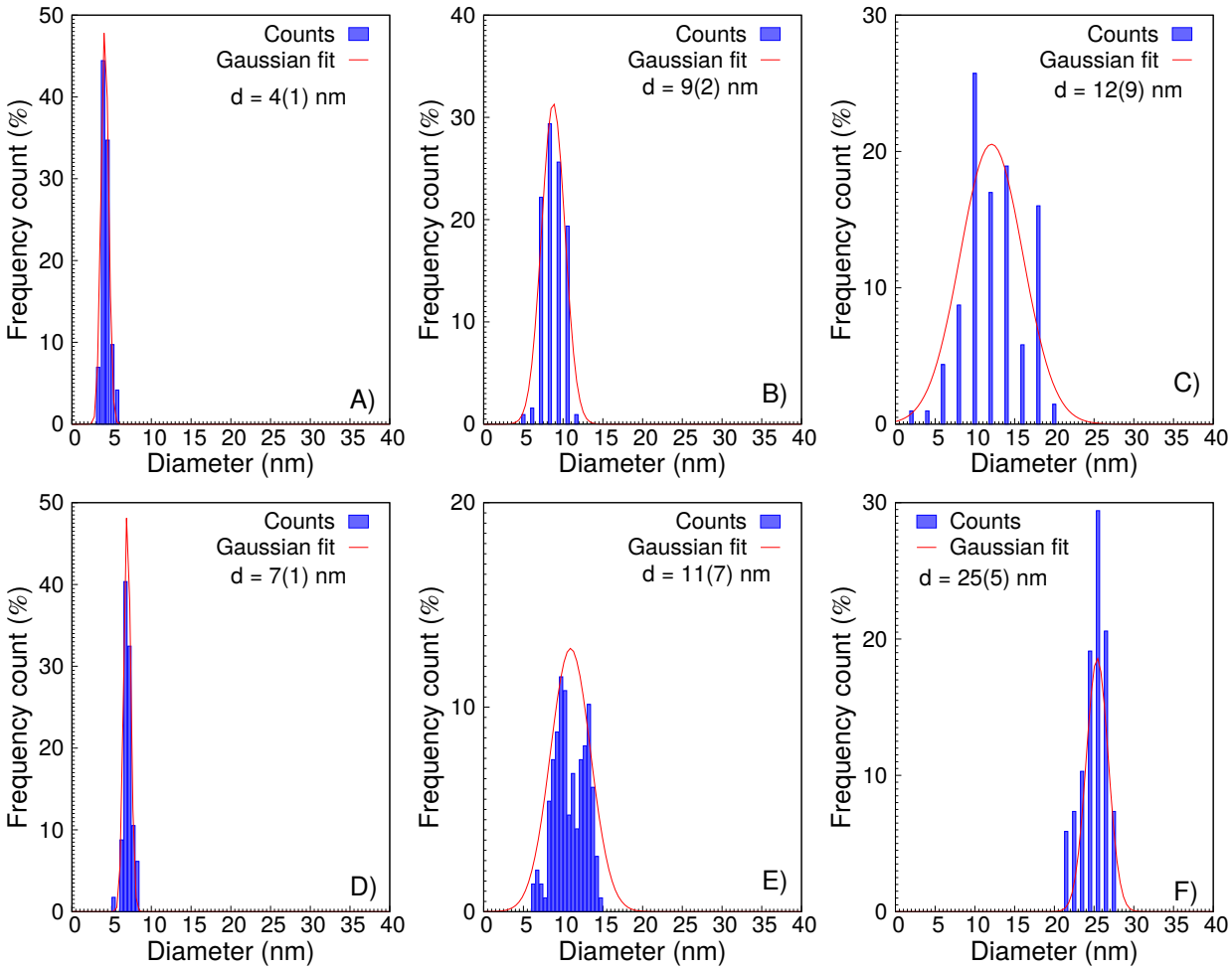

Figure 3: Particle size statistics from TEM images of the α-$NaYF_4$ NPs with histograms fitted to Gaussian distributions. The mean sizes are indicated with the FWHM of the Gaussian distribution fitted to the data indicated in parenthesis.

3.2 ^{23}Na solid state NMR

Fig. 4 shows the room temperature ^{23}Na SP-MAS spectra of the NPs and respective deconvolutions. The spectrum of the NP F extends from -5 to -30 ppm with the center of gravity at -18.8 ppm. It is comparable to the spectra reported by Arnold et al.,[12] obtained for NPs of similar size. In the regime of "fast" MAS, a ^{23}Na isotope should resonate at a frequency shift that is a composition of the isotropic chemical shift (δ_{CS}^{iso}) and the quadrupolar isotropic shift (δ_{Q}^{iso}), i.e., according to $\delta_{CG} = \delta_{CS}^{iso} + \delta_{Q}^{iso}$. The line broadening should be dominated by the second-order term of the quadrupolar coupling since dipolar interactions and chemical

shift anisotropy would be averaged out by the MAS. We have measured NP B and NP F at various MAS (see Supporting Information, SI),[27] and around a MAS of 5 kHz the spectra show resolution similar to the ones at MAS of 15 kHz, which is already at the highest possible resolution.

Arnold et al.[12] assumed the condition of "fast" MAS at 25 kHz, and that second order quadrupole broadening is of secondary importance (considering the cubic structure). From quantum chemical calculations and the measurements at different magnetic fields they attributed most of the spectral broadening to the chemical shift distributions due to local dissimilarities around the ^{23}Na, as following: Around the Na atoms there are eight possible nearest neighbors (n.n.) and twelve near to nearest neighbors (n.n.n.). The n.n. are F atoms or vacancies, and the n.n.n. are Na or Y atoms. The Na and Y are statistically distributed such that the observed ^{23}Na can have 3 Na and 9 Y atoms in the second coordination sphere, or 4 Na and 8 Y, and so on (F vacancies are not noted for the undoped NP and Na/Y vacancies are considered negligible). The differences in the Na site with respect to the n.n.n. are the main reason for the spectral broadening due to a distribution of isotropic chemical shift. They interpreted their quantum chemical results correlating the chemical shifts at higher frequencies (around -10 ppm) to the rich Na coordinated sites (approximately 8 Na and 4 Y atoms), and at lower frequencies (around -20 ppm) to the poorly occupied Na coordinated sites. However, the correlation is not so obvious (see Fig. S.1 of Ref. 12), as pointed out by the authors themselves. For example, an observed ^{23}Na with 7 Na neighbors appears over the whole range of chemical shifts. Thus, the line broadening is correctly associated to the statistical distribution of Na and Y atoms in the cubic lattice of the α-$NaYF_4$ NPs (resulting in a $\Delta\delta_{CS}^{iso}$), but it should be also affected by local distortions generated by such a distribution (resulting in a $\Delta\delta_{Q}^{iso}$, as discussed below).¶ Second order quadrupolar broadening maybe be hidden by these local inhomogeneities, since the structure approaches to the cubic one.

Now, assuming the presence of slightly distinct Na sites in the α-$NaYF_4$ lattice (with

¶Note that Δ usually represents the chemical shift anisotropy. Here Δ refers to a distribution of isotropic chemical shift ($\Delta\delta_{CS}^{iso}$) and quadrupolar shift ($\Delta\delta_{Q}^{iso}$).

respect to the Y/Na ratio in the neighborhood and local distortions from the cubic structure), the spectra should be simulated by a composition (convolution) of Lorentzian resonances representing each site. In this approach we are neglecting anisotropic terms coming from the anisotropic chemical shift and second order quadrupolar coupling. The first term is averaged out by the fast MAS and the second order quadrupolar broadening is small in comparison with the chemical shift distribution, as discussed below. This more formal treatment of the NMR resonance lines as compositions of Lorentzian resonances and further Gaussian distribution envelope, done in two steps, are demonstrated in the appendix. Alternatively, one may also represent an inhomogeneous line broadening by combining Lorentzian and Gaussian distribution representing different sites in one Lorentzian/Gaussian envelop. In this context, a larger amount of Gaussian over Lorentzian weights mean a broader distribution of Na sites with respect to their local structure (distortions) or Na/Y ratios. We used this approach in this work, due to its simplicity and because both approaches lead to the same conclusions.

There are few differences between the spectra of the undoped NP measured by Arnold et al.[12] and of the NP F reported here. The spectrum of the NP F can also be described by an envelope with three features, here simulated by three distributions composed by combinations of Gaussian and Lorentzian distributions. The best fit is obtained by combining X=0.6 with Gaussian and $1 - X$=0.4 Lorentzian; (refer to Table 2 for deconvolution details). Note that the three features do not assign distinguishable ^{23}Na sites, but they appear as an overlap of many contributions. Our spectrum is slightly narrower then the one reported by Arnold et al.,[12] despite their higher MAS and magnetic field. This is possibly due to the less (or absent) contamination or spurious phases and narrower particle size distribution in our NP F, in contrast to the particles studied by Arnold et al.[12] (for instance σ_{FWHM} is 5 nm for NP F and approximately 8 nm in Ref. 12). Furthermore, our spectrum is shifted by approximately 7 ppm to higher frequencies (by visually interpolating their data to ν_0 = 132.2 MHz). This apparent difference is due to their choice of referencing solid NaCl at 0 ppm, and not the

conventional NaCl 1M aqueous solution at 0 ppm and solid NaCl at 7.21 ppm.

The ^{23}Na NMR spectra change considerably for the NPs smaller than the NP F. The spectrum of the NP E, for instance, can be fairly well represented by two distinguishable signals: An intense and broad peak around -18 ppm and a small peak at -6 ppm (with a contribution of 4% for the integrated intensity). The X is 0.8 for the peak around -18 ppm and 0 for the peak at -6 ppm, meaning that the former signal has a higher Gaussian contribution (Table 2), thus, with more ^{23}Na site variations. As the NPs become smaller and/or with higher polydispersity, the small peak around -6 ppm becomes more prominent and can be distinguished around -9 ppm instead. Interestingly, NP A, the smallest one, shows an extended band to even higher frequencies (around 0 ppm). As further validated below, the wide peak around -18 ppm represents the ^{23}Na in the bulk of the NPs A-E with the site variations similar to those described by Arnold et al.[12] This peak contains all the features displayed for NP F, though less distinguishable, related to the smaller particle sizes. The small peak at higher frequency, around -6 ppm (or -9 ppm), is associated to the higher surface/bulk ratio (and/or polydispersity) and can be interpreted as Na surface sites or sites nearby defects.

For the ^{23}Na spectra of the NPs among those with higher polydispersity, NPs B, C and E, the contribution from the peak at -9 ppm is 21, 16, and 4%, respectively. Accordingly, the contribution from the sites assigned as surface or nearby defects decrease as particle size increases. A similar trend can be drawn for the NPs with low polydispersity, NPs A, D and F: While no signal related to surface/defect sites are attributed to the NP F, for NP D and A this peak contributes with 5 and 11%, respectively. Finally, we can compare the two smallest NPs with low and high polydispersity: NP A has 11% of contribution from surface/defect sites, while NP B has 21%. Although NP B is, on average, larger than NP A, the surface effects or defect sites on the former are more noticeable. It means that these sites are also related to polydispersity, i.e., the experimental conditions that lead to higher polydispersity also lead to higher probabilities of Na sites nearby defects.

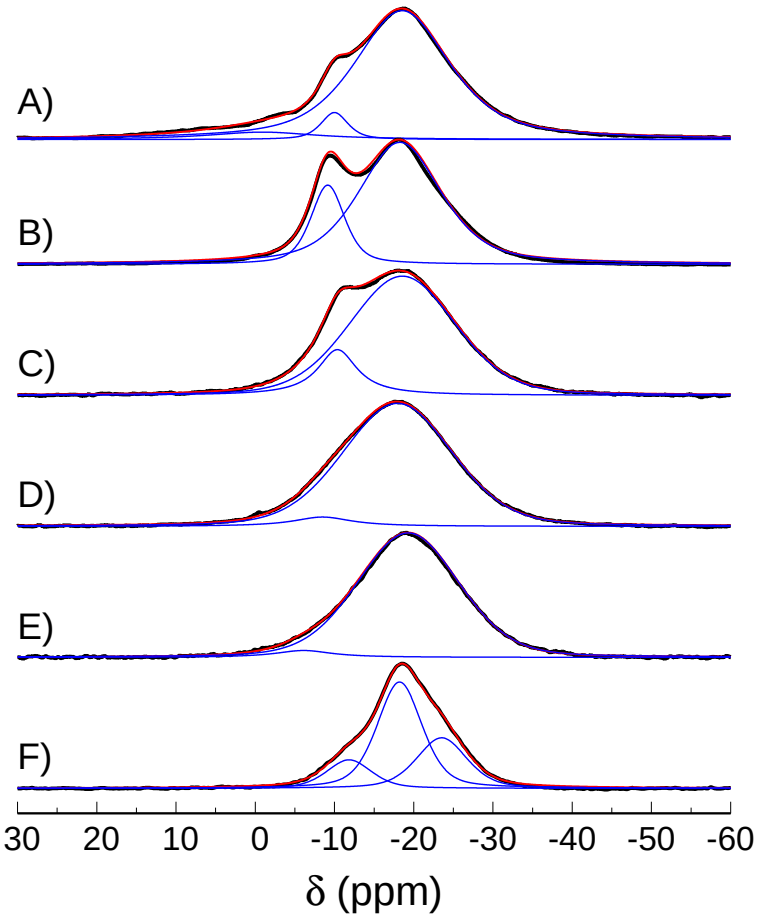

Figure 4: ^{23}Na SP-MAS spectra and respective deconvolutions of the NPs. See Table 2 for deconvolution details. The detected resonances are mostly from CT due to selective excitation.

Fig. 5 shows the inversion recovery spectra of representative samples, NPs A, B, D, and F, recorded after several delay times between the inversion pulse (π) and the excitation pulse ($\pi/2$). For each NP, the spectra recorded after an inter-pulse delay time of 1 s resemble those obtained from the SP-MAS, because they were recorded after full relaxation. However, for NP A and, most remarkably for NP B, the peak at -9 ppm becomes more pronounced for shorter evolution times. With the NP B for instance, this peak turns into the most intense for delay times as short as 46 ms. Therefore, the resonance signal at -9 ppm has a much shorter spin-lattice relaxation time. Similar behavior is observed for the NPs C (not shown), D, and E (not shown), although with the peak around -9 ppm less pronounced. For NP F, the inversion recovery spectra are nearly independent of evolution times, indicating for

Table 2: Best fitting parameters from numerical deconvolution of the ^{23}Na SP-MAS spectra of the NPs.

NP	δ(ppm)	σ_{FWHM}(ppm)	X(G,L)*	A(%)**	δ(ppm)	σ_{FWHM}(ppm)	X(G,L)*	A(%)**	δ(ppm)	σ_{FWHM}(ppm)	X(G,L)*	A(%)**
A	-1.3	19.3	0.5	6	-10.0	4.0	0.5	5	-18.5	14.1	0.4	89
B	-	-	-	-	-9.1	5.0	0.5	21	-18.2	12.2	0.5	79
C	-	-	-	-	-10.4	6.0	0.0	16	-18.6	15.7	0.8	84
D	-	-	-	-	-8.5	8.8	0.0	5	-17.9	16.2	0.8	95
E	-	-	-	-	-6.1	8.6	0.0	4	-19.3	15.1	0.8	96
F***	-11.8	6.6	0.6	15	-18.2	6.7	0.6	56	-23.5	7.4	0.6	29

*X(G,L) means the ratio between Gaussian (X) and Lorentzian ($1-X$) in the curve, i.e., X=0 stands for a full Lorentzian distribution and X=1 for a full Gaussian distribution. **A(%) is the contribution in area of the peak to the whole spectrum. ***Note that for NP F the three deconvoluting peaks describe a superposition of chemical shifts due to the ^{23}Na local site variations in the bulk of the NP, as detailed in the manuscript, and they are not attributed to surface effects or defects. This interpretation is based on the quantum chemical calculations performed in ref. 12 and our relaxation results. It is a coincidence that such a superposition of chemical shifts results in a band with three features that can be represented by three Gaussian/Lorenztian distributions.

negligible effects from the surface or defective sites in comparison to the bulk ones (Fig. 5).

There are numerous effects influencing the ^{23}Na longitudinal relaxation.[28,29] In general, the longitudinal relaxation of quadrupolar nuclei are not single exponential, but governed by 2I rates.[30,31] The initial excitation conditions also influence the observed magnetic relaxation, particularly, differentiating the situations of complete saturation of both CT and satellite transitions (STs), from the selective saturation of the CT.[29,30,32–34] In the latter case, as approximately in our experiments, the return to equilibrium of the magnetization can be described by only I+1/2 rates (if 2I is odd).[30] The (I+1/2)-exponential behavior of the relaxation is a function of the spin-lattice transition probabilities involving single- and double-quantum processes, $W_1 = W(m = 1)$ and $W_2 = W(m = 2)$, which themselves depend on the specific form of the relaxation mechanism and are functions of temperature and crystal orientation.[30] Next, the relaxation process might be due to fluctuations of the dipolar couplings (magnetic relaxation) and/or to the quadrupolar coupling to the time-modulated EFG (quadrupolar relaxation).[35] The first mechanism is observed in cubic structures or for nuclei with small quadrupole moment. The second mechanism is dominant in imperfect cubic and more distorted structures and an interplay of both effects is also possible.[35] For a crystallite under fast MAS, i.e., when the rotor period is much shorter than T_1, the orien-

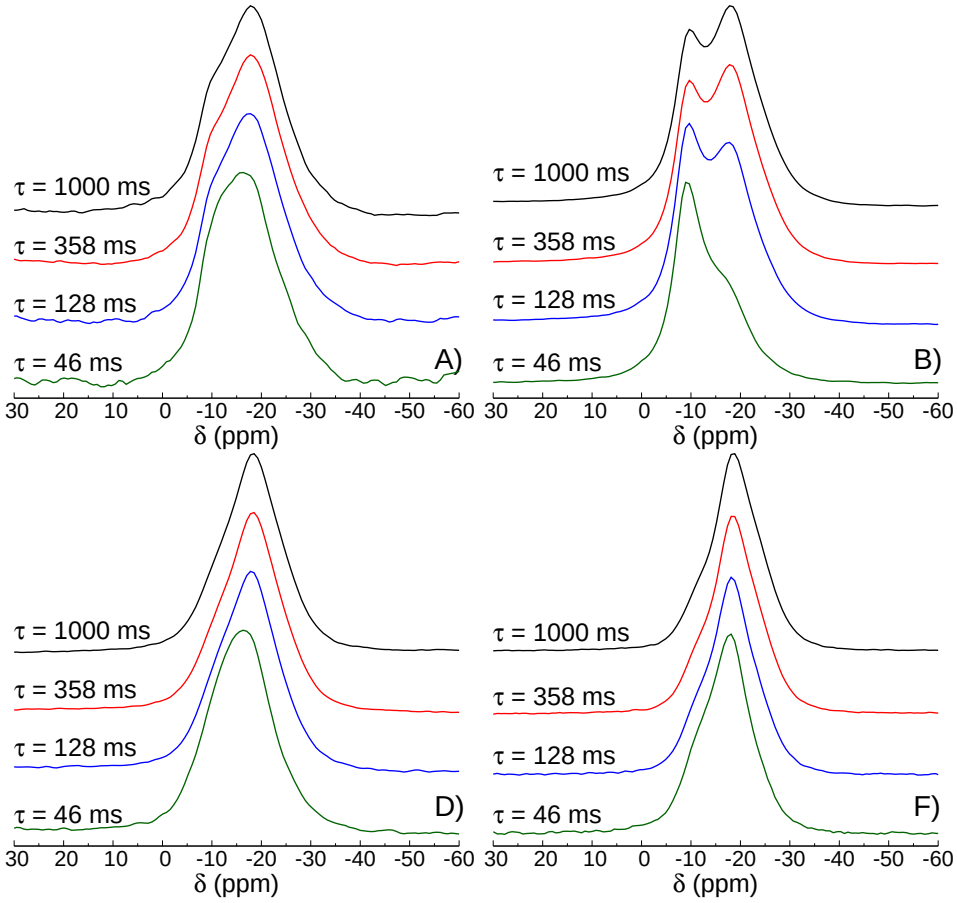

Figure 5: Inversion recovery spectra of NPs A, B, D, and F, obtained after various inter-pulse delay times. The spectra of NPs C and E do not contribute further to the discussion and are omitted. The detected resonances are mostly from CT due to selective excitation.

tational dependence of the transition rates are averaged to a characteristic value (W_1^{avg} and W_2^{avg}).[36] The statement holds approximately for polycrystalline samples.[36] For perfect cubic crystals (and sometimes also for imperfect cubic crystals), W_1^{avg} can be regarded as equal to W_2^{avg}, and the relaxation behavior approaches a single exponential.[30,37–40] In addition, MAS activates zero-crossing conditions between ST and CT during the rotation periods (first-order spin-exchange transitions),[28,29,32,34] adding a further relaxation channel, increasing the apparent magnetic relaxation rate.[34] On top of that, the local distortions in the ^{23}Na sites of the α-$NaYF_4$ NPs, as previously described, would lead to a distribution of relaxation rates, adding further dispersion in the magnetization recovery data.

Our experimental method does not allow to discriminate the different contributions to

the relaxation patterns, neither it is in the scope of this work. However, our results highlight the main mechanism that drives the differences in the longitudinal magnetization dynamics between the two characteristic ^{23}Na sites, surface or defects in contrast to bulk sites. Based on the typical relaxation times found for the studied NPs, comparable to similar structures in terms of quadrupolar coupling,[41,42] the changes in longitudinal relaxation at room temperature for the α-$NaYF_4$ NPs are mainly driven by the quadrupole mechanism.[35,43] The considerable EFG are created by local distortions and the modulation of the quadrupole coupling by lattice vibrations, especially for ^{23}Na sites in the bulk. One expects faster relaxation times for the sites on the surface and/or defects, given that the nuclear motion and impurities as protons from adsorbed water are also contributing to the relaxation of the magnetization.[33,44,45]

We can assign T_1 as the characteristic time in which the magnetization returns to equilibrium after a selective CT inversion, according to:

$$M_z(\tau) = M_0\{1 - f[e^{-(\frac{\tau}{T_1})^{\lambda}}]\}, \quad (1)$$

where M_0 is the initial magnetization, $f < 2$ accounts for incomplete M_0 inversion after the π pulse, and λ accounts for differences between W_1 and W_2 (though we assume $W_1 \sim W_2$, considering the pseudo-cubic structure of the NPs),[30] the contribution from spin exchange transitions and the dispersion of these relaxation rates due to local distortions and inhomogeneities caused by surface/bulk interface.

Fig. 6 shows the integrated intensity of the deconvoluted peaks as a function of τ for all studied NPs. The adjusted curves, according to Equation (1), are in good agreement with the experimental data (the obtained parameters are indicated in Table 3). The signals around -9 ppm exhibit T_1 of 17 ms for NP A and within 1-3.5 ms for NPs B, C, D, and E. The signals around -18 ppm show T_1 more than one order of magnitude longer, within 50-125 ms, except for NP A, which shows a more moderate difference in T_1.

Since the NPs present only cubic crystallographic phase (as observed by XRD), though

locally distorted, the signal around -18 ppm with longer relaxation times is attributed to ^{23}Na in the bulk sites of the nanoparticles. The peak around -9 ppm with shorter relaxation times are related to sodium atoms on the surface or nearby defects. Considering that the dominant spin-lattice relaxation mechanism is the quadrupole coupling to the time modulated EFG, and that the quadrupolar coupling of both sites are quite similar (see 3Q-MAS results below), the differences in relaxation times must be associated to the dynamics of the EFG. The surface sites and/or sites nearby defects demonstrate a more intense fluctuation of the EFG, caused by thermal lattice vibrations (spin-phonon interactions) and the motion of defects, oleic acid molecules attached to the yttrium sites on the surface[46] and polar sorbate molecules[44,45] (as in the external layers of the nanoparticles). As expected, the NP F presents the longest spin-lattice relaxation, 125 ms, for the peak at -18 ppm, indicating that the bulk structure of the largest particle is also the most symmetric one.

Table 3: Fitting parameters according to Equation (1) of deconvoluted ^{23}Na inversion recovery integrated intensity as a function of inter-pulse delay time.

Parameter	NP A	NP B	NP C	NP D	NP E	NP F
$T_1^{(-9ppm)}$ (ms)	17(3)	0.9(3)	3.4(6)	2.1(1)	1.3(9)	–
$\lambda^{(-9ppm)}$	0.34(2)	0.45(6)	0.45(4)	0.7(3)	0.5(1)	–
$f^{(-9ppm)}$	1.44(8)	1.43(1)	1.70(1)	1.69(1)	1.70(1)	–
$T_1^{(-18ppm)}$ (ms)	74(1)	51.2(6)	90.4(6)	45.2(5)	90.0(7)	125(2)
$\lambda^{(-18ppm)}$	0.65(1)	0.52(1)	0.64(1)	0.57(1)	0.60(1)	0.65(1)
$f^{(-18ppm)}$	1.36(1)	1.9(3)	2.0(1)	1.4(5)	1.5(4)	1.17(1)

In order to further investigate the structural differences of the sites attributed to the surface and/or defects and bulk sites, we performed 3Q-MAS. In the well established 3Q-MAS experiments,[18,19] it is possible to resolve the contribution from δ_{CS}^{iso} and δ_{Q}^{iso} to the total shift δ_{CG} of the MAS NMR spectrum. Succinctly, this is done by composing the signal from appropriate instant frames after echo pulses that access single and triple coherences in which anisotropic terms on the system evolution are canceled out.[18,19] Thus, the regular MAS spectrum is collected in the direct dimension (F2) and correlated to an isotropic spectrum obtained in the indirect dimension (F1). After a shear transformation in F1, these shifts are

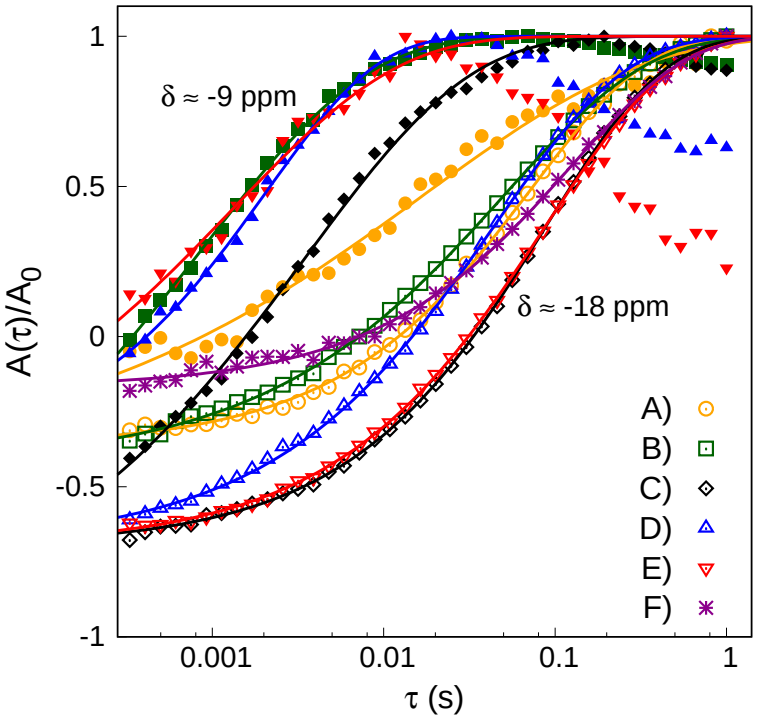

Figure 6: ^{23}Na inversion recovery integrated intensity as a function of inter-pulse delay time and fits according to Equation (1) for all NPs. Solid symbols are due to the signal at -9 ppm and open symbols to the signal at -18 ppm. Note that the signals at -9 ppm show a decrease in intensity at long inter-pulse delay times ($\tau \geq 0.02$ s). This effect is more pronounced for the NPs that present the smallest ratios between the surface or defect signals with respect to bulk signals ($A(\delta_{-9ppm})/ A(\delta_{-18ppm})$). These downturns occur because the peaks representing the bulk sites dominate the spectra at long delay times, obscuring the small peaks at -9 ppm which are underestimated in the deconvolution.

described by:[47,48]

$$\delta_{F1} = \delta_{CS}^{iso} - \frac{10}{17}\delta_{Q}^{iso}, \tag{2}$$

which yield,

$$\delta_{CS}^{iso} = \frac{17}{27}\delta_{F1} + \frac{10}{27}\delta_{CG}. \tag{3}$$

From δ_{Q}^{iso} it is possible to calculate the second-order quadrupolar effect parameter (P_Q), since

$$\delta_Q^{iso} = -\frac{P_Q^2}{\nu_0^2}\beta(I) \cdot 10^6 \quad (4)$$

with

$$\beta(I) = \frac{204}{680}\frac{[I(I+1) - 3/4]}{[2I(2I-1)]^2} \quad (5)$$

which is a measure of the magnitude of the EFG[49] (ν_0 is the Larmor frequency and I is the nuclear spin number).

Fig. 7 shows the 3Q-MAS spectra of representative samples, NPs A, B, D, and F, with projections on the isotropic dimension (F1) taken from the slice when the direct dimension (F2) is around -18 ppm (in blue, on top) and -9 ppm (in red, on bottom). For the NP A, the most intense signal at -18 ppm is correlated to an isotropic signal at -15 ppm. The shoulder observed in the direct dimension at -10 ppm is correlated to an isotropic signal at -8.6 ppm with a shoulder around -4 ppm. This is also observed for the NP B, with the small shoulder around -4 ppm in the isotropic dimension even more visible. The contribution from lower frequencies is less remarkable for the other nanoparticles (NPs D and F), but a small isotropic peak around -6 ppm remains distinguishable when the peak around -9 ppm in the direct dimension is projected onto the isotropic dimension.

The calculated isotropic chemical shift of the bulk site is around -16 ppm for all samples and around -8 ppm for the surface sites and/or defects.[47] The calculated quadrupolar coupling constant for bulk sites are small, and ranges about 1.2-1.0 MHz, as also previously estimated.[12] It is slightly smaller for the surface/defect sites, around 0.4-1.1 MHz, and slightly higher for the shoulder extending to higher frequencies, around 1.6-2.0 MHz. These estimates are taken from the line broadening in the direct and indirect dimensions. The similar EFG between the sites, within their ranges, indicates that the site distortions in both environments are not substantial.

Fig. 8 shows the field dependence of the ^{23}Na SP-MAS spectra at 15 kHz with respective deconvolutions for NPs A and F. As expected, the low field spectra taken at ν_0 = 64.1

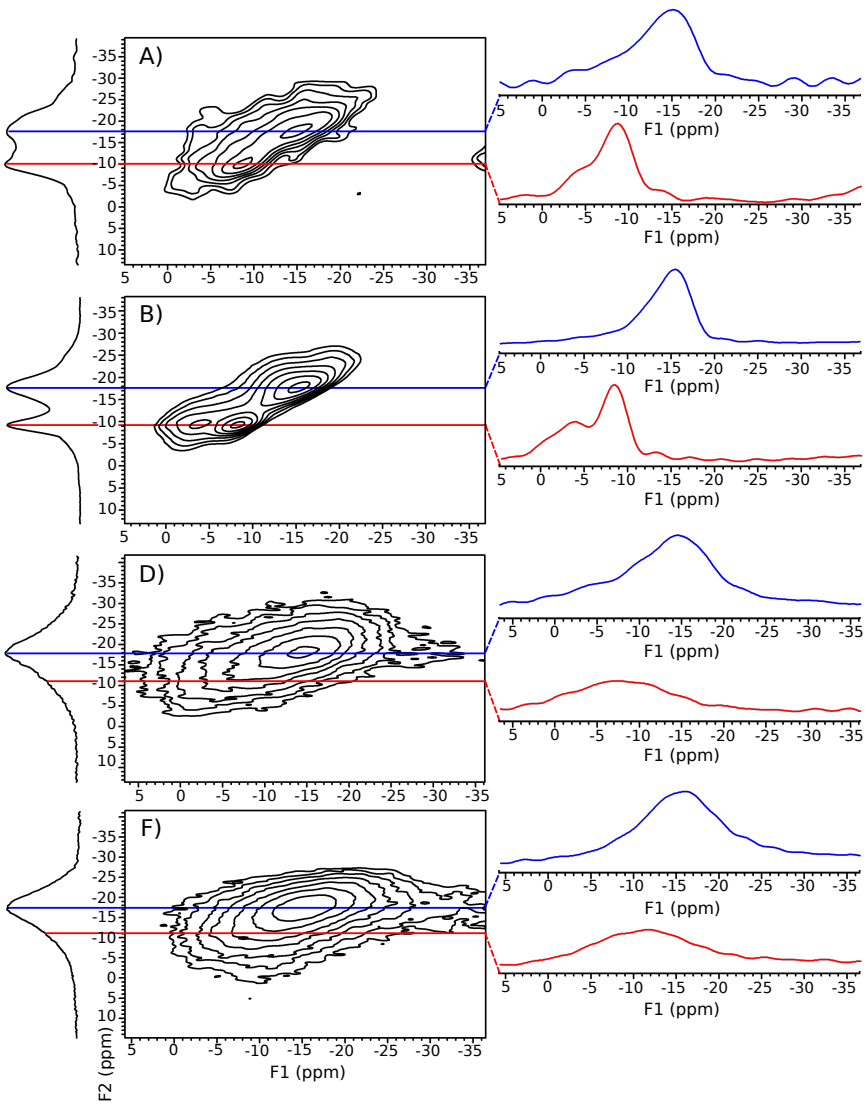

Figure 7: ^{23}Na 3Q-MAS spectra of the representative samples, NPs A, B, D, and F, with projection of the signal attributed to the bulk of the NPs (≈ -18 ppm) onto the isotropic dimension (in blue) and projection of the signal attributed to the surface/defects (≈ -10 ppm, in red).

MHz (B_0 = 5.64 T) are the broadest ones and extend from -5 to -70 ppm. Mostly because the spectra are compositions of chemical and quadrupolar shifts, and the line broadening is proportional to the $\Delta\delta^{iso}_{CS}$+$\Delta\delta^{iso}_{Q}$. Since δ^{iso}_{Q} is proportional to P_Q^2/ν_0^2 (Eq. 6), at low field (and thus low ν_0) the distribution of P_Q between the sites is evidenced ($\Delta_Q \sim 1/\nu_0^2$). In addition, the broadening of the central transition line is inversely proportional to B_0 in second order quadrupolar coupling (not averaged out by the MAS).[50] This contribution

depends on the asymmetric parameter of the EFG and it is probably less important since the structure identified by XRD is cubic, though locally distorted. The spectra of both samples are similar, but for NP A there is an enhanced shoulder around -10 ppm and a small contribution extending up to 15 ppm, which are contributions from surface/defect sites. The spectra taken with $\nu_0 = 158.8$ MHz ($B_0 = 14.1$ T) are similar to the previous ones with $\nu_0 = 132.2$ MHz ($B_0 = 11.7$ T) except that the signal attributed to the bulk sites becomes closer to the peak attributed to the surface/defect sites. The smaller shift of the peaks attributed to surface and/or defects as magnetic field increases indicates a smaller quadrupolar coupling, as obtained from the 3Q-MAS experiments. From the center of gravity of the spectra at $B_0 = 5.64$ T, and taking the assigned peaks for other magnetic fields, the ^{23}Na in the bulk and surface sites or nearby defects of NP A demonstrate a P_Q of 1.8(4) and 0.4(2) MHz, respectively, with a δ_{CS}^{iso} of -14.1(5) and -9.0(2) ppm (see data fit to Eq. 2 in combination with Eq. 4 and 5 in the SI).[27] For NP F, the δ_{CS}^{iso} is -14.76(4) ppm and P_Q is 1.7(1) MHz, in agreement with the 3Q-MAS experiments.

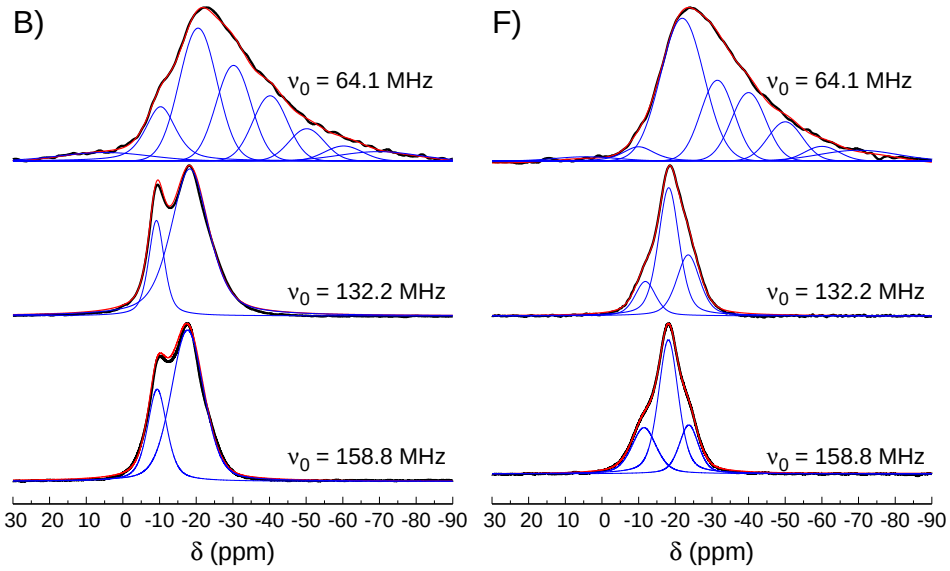

Figure 8: Field dependence of the ^{23}Na SP-MAS spectra at 15 kHz and respective deconvolutions for representative NPs A and F. The detected resonances are mostly from CT due to selective excitation.

Overall, our results can be analyzed as follows: The ^{23}Na spectra of the NPs present a broad peak at -18 ppm due to the α-$NaYF_4$ bulk phase. The spectral broadening is

dominated by the chemical shift distribution associated with Na sites that are different relative to first and second neighbors,[12] in addition to slight local site distortions from the cubic lattice, resulting in a distribution of quadrupolar shift. Upon decreasing the size of the NPs to less than 10 nm, another low-field (high frequency) signal emerges, implying the presence of a less shielded environment. The large difference in spin-lattice relaxation rates between bulk and surface sites can not be explained only by the different EFG in these regions. It has to be associated with the dynamics (fluctuations) of the EFG related to distinct vibrational modes in the bulk and surface sites.[45,51,52] The increased mobility of Na ions is also observed for confined $NaNO_2$ in nanoporous materials,[53,54] which have the same size scale as the NPs investigated here. Thus, ionic motion in the surface sites of the NPs might also play a role in the relaxation rates.

Interesting studies in a similar fashion as ours have been reported. For semiconducting nanoparticles such as CdSe (a closer system to the one presented here) Thayet and collaborators[55] have also observed a ^{77}Se line broadening and possibly spectral resolution for "bulk" and "surface" sites via relaxation time analyses in the same fashion as reported here. They have interpreted that the paramagnetic contribution to the chemical shielding is attenuated in small particles due to their higher energy gap, leading to shifted resonance lines.[55] In addition, the structural differences between the bulk and surface in the NPs are also analyzed in a general way by taking into account the site distortions at the surface for other nanoparticles.[56,57] Lo et al.[58] have found similar results for LaF_3 NPs with sizes of 8-10 nm, but only a line broadening was noticed in the ^{139}La and ^{19}F spectra when compared to the bulk materials. Their spectra do not display sufficient resolution to distinguish bulk from surface site contributions, although a bi-exponential behavior of T_1 was justified by surface effects. They observed longitudinal relaxation times approximately 2 orders of magnitude shorter than that of bulk samples, with the relaxation process driven by quadrupole interactions in addition to a small influence of paramagnetic impurities. Perhaps studies in smaller LaF_3 NPs would lead to a discernible spectral and relaxation time resolutions as those reported

in this work.

3.3 ^{19}F solid state NMR

Fig. 9 shows the ^{19}F SE-MAS spectra of all NPs. The spectrum of NP F, for instance, shows a broad peak centered at -75 ppm, extending from approximately -50 to -95 ppm, with a small shoulder around -120 ppm, accounting for 1% of the integrated intensity. The dominant peak can be represented by 3 Gaussian/Lorenztian peaks (see deconvolution details in the SI).[27]) This spectrum is very similar to that of Arnold et al. for the undoped α-$NaYF_4$ NP,[12] and approximately 10 ppm shifted to higher frequencies relative to the one obtained by Bessada et al.[59] for bulk α-$NaYF_4$ (centered at -85 ppm). From quantum chemical calculations, Arnold et al.[12] assigned the ^{19}F resonances to defects free α-$NaYF_4$, where the fluorine is four-fold coordinated as FNa_xY_{4-x} (x = 0, 1, 2, 3, 4). The resonances at high frequencies are related to Na-rich sites (around 0 ppm), the ones at low frequencies to Y-rich sites (around -75 ppm), and those at intermediate frequencies (around -50 ppm) to sites with similar Na/Y ratios in addition to an overlap of the two sites previously described. The main peak in the NP F spectrum can be interpreted according to Arnold et al.[12] Again, the spectral line broadening is attributed to a distribution of δ_{CS}^{iso} due to local site variations coming from variable Na/Y cell occupancies. At the MAS employed here, this effect dominates over the anisotropic chemical shift (and distributions) and dipolar broadening. In fact, the spin-spin relaxation time of the main peak is around 0.7 ms (SI)[27] corresponding to a homogeneous broadening of only 0.5 kHz, while its σ_{FWHM} is $\approx$ 7 kHz.

The interpretation of the small shoulder at -120 ppm is grounded on the work of Bessada et al.[59] in NaF-YF_3 melts. The ^{19}F resonance of the stoichiometric $NaYF_4$ melt is observed around -75 ppm, while in YF_3 rich compositions the ^{19}F resonances are observed at higher frequencies and in NaF rich compositions at lower frequencies. The resonances at -120 ppm are noticed for NaF-YF_3 melts with molar contents of 0.3 for the YF_3 and 0.7 for the NaF. In order to form a α-$NaYF_4$ structure with such stoichiometry (as confirmed from the XRD and

^{23}Na NMR results), it is necessary to form fluorine deficient sites. Thus, the small shoulder at -120 ppm is assigned to fluorine in Na-rich sites of the α-$NaYF_4$ structure in the presence of fluorine vacancies. This indicates for the presence of mobile fluorines, first suggested by Roy and Roy.[10] Accordingly, this peak has longer spin-spin relaxation times in comparison to that at -75 ppm ($\approx$ 1 ms, see SI).[27]

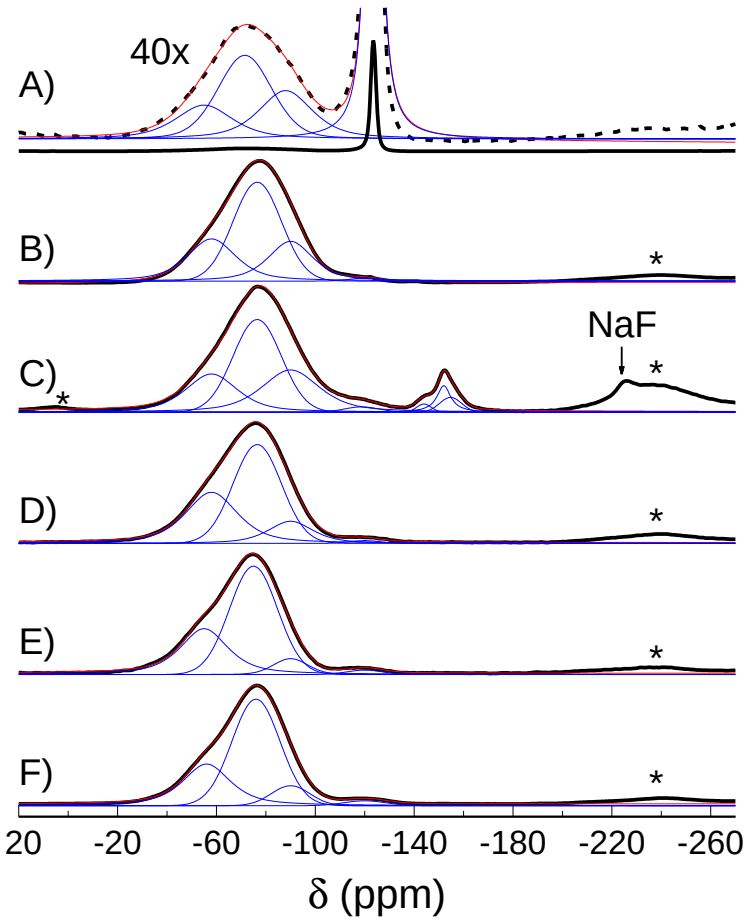

Figure 9: ^{19}F SE-MAS spectra and respective deconvolutions of all NPs studied, taken after 56 μs inter-pulse delay time. Spinning sidebands are indicated by asterisks. The deconvolutions, presented in the SI,[27] are not considering the spinning sidebands due to their low intensity ($\leq$ 1%, except for NP C), and because the detailed quantitative information of this contribution is not relevant for the discussion.

The NPs E, D, and B present ^{19}F spectra similar to the NP F. The spectrum of NP C shows additional resonances around -150 ppm and -224 ppm, contributing to $\approx$ 10% and 1% of the spectrum weight, respectively. The resonances around -150 ppm are tentatively attributed to additional species of free fluorine in Na-rich NaF-YF_3 composition ($YF_3 \leq$

20%),[59] possibly as amorphous structures formed in the crystal interstices (since they are not detected by XRD). The peak at -224 ppm is due to remaining NaF present in the NP despite the extensive washing procedure of the NP.

The ^{19}F spectrum of the NP A is the most distinct one. It has approximately 75% of the spectrum composed by the peak at -120 ppm and a broadening in the peak at -75 ppm attributed to the stoichiometric α-$NaYF_4$. Thus, ≈75% of the fluorines are attributed to fluorine in Na-rich sites and, consequently, the broadening in the peak around -75 ppm is due to the presence of Y-rich sites and fluorine vacancies.

Interestingly, the indication of small contents of fluorine vacancies for NPs B-F (≈ 1%) and high contents for the NP A (≈ 75%) points to fluorine ionic motion,[60] as previously predicted.[61,62] The easy decoupling between ^{23}Na and ^{19}F in our measurements also indicates fast motion of fluorines. For instance, the ^{23}Na-^{19}F dipolar coupling is estimated as 4-6 kHz for static nuclei in the unit cell, while ≈ 5 kHz of MAS was sufficient to average out this interaction in the ^{23}Na spectra (see SI).[27] Temperature dependent NMR is a promising lead to characterize the ion conductivity in the α-$NaYF_4$ NPs, particularly, because ion mobility might be largely enhanced in small NPs.[63] Note, however, that line broadening will not be the appropriate parameter to probe such dynamics since the spectra of the NPs are dominated by inhomogeneous broadening. Therefore, the relaxation rates obtained from echo experiments will rather be the most suitable parameter to characterize ion mobility as a function of particle size and polydispersity.

4 Conclusions

We synthesized and characterized cubic α-$NaYF_4$ nanoparticles in a wide range of particle sizes (4-25 nm). We carried out a systematic method to evaluate site differences in nanoparticles due to defects and surface effects, combining various and very sensitive NMR techniques. ^{23}Na and ^{19}F were used as local probes for the site-selective spectral analysis, spin-lattice

and spin-spin relaxation times, and multi-quantum experiments. Upon varying the nanoparticle size and carrying out these locally sensitive experiments, we were able to unveil small but not less important structural changes due to surface effects in this particular system. Moreover, the presented methodology may be extended to other nanoparticle systems. The structural effects are more prominent in the smallest particles ($\phi \lesssim 7$ nm), especially when the preparation conditions lead to broader particle size distribution ($\sigma_{FWHM} \gtrsim 20\%$ of their mean size). This is important when site symmetry breaking is desired while avoiding defects, as for upconversion host systems used for technological applications.

A NMR spectra simulated as a Gaussian distribution of Lorentzian resonance lines

Fig. 10 shows the spectra of the NPs B (left) and F (right) simulated by a sum of Lorentzian resonances spaced 1 ppm apart using a fixed width of 2.5 ppm. The linewidth was chosen according to the shortest spin-spin relaxation time of the ^{23}Na in the different sites, 1 ms, estimated from SE-MAS experiments (see SI).[27] The shift of 1 ppm between Lorentzian resonances was chosen to reproduce the smoothness of the experimental spectra. The amplitudes of the Lorentzian resonances were plotted as a function of chemical shift, and these data were simulated by two Gaussian distributions (inset to Fig. 10). For NP B, the Gaussian distributions are centered at -9.0 and -18.2 ppm, with weight contributions of 22 and 78%, respectively. For NP F the Gaussian lines are centered at -10.1 and -19.5 ppm, with weight contributions of 6 and 94%, respectively. This data analysis corresponds to the following interpretation: The Na sites of either bulk or surfaces of the NPs are composed by sites that are slightly different due to distortions or Na/Y neighboring composition. Each site has a first order spin-spin relaxation, as expected, due to dipolar and quadrupolar interactions. Thus, each site contributes to a Lorentzian resonance signal. However, the sites show a chemical shift and quadrupolar shift distribution, which is better represented by a Gaus-

sian distribution of sharp Lorentzian lines. The surface/bulk ratio obtained by this rigorous method is similar to that obtained by combining Gaussian and Lorentzian distributions, as described in the manuscript. For instance, the SP-MAS spectrum of the NP B presents 21% of contribution from the peak centered at -9.1 ppm and 79% from the peak at -18.2 ppm (Table 2).

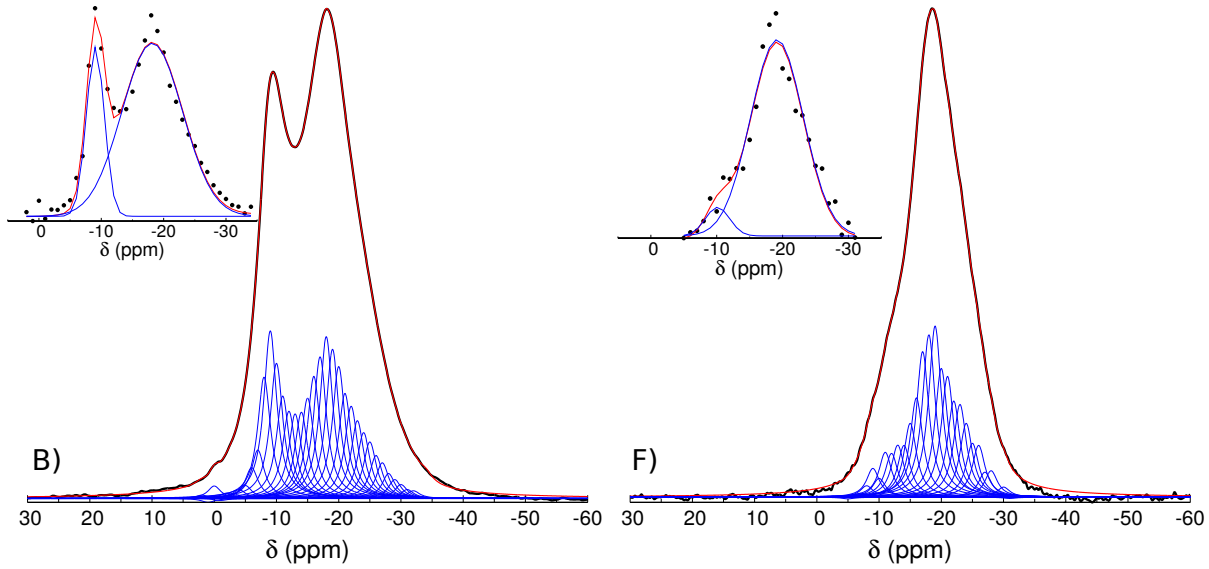

Figure 10: ^{23}Na SP-MAS spectra of the NPs B and F and deconvolutions as an envelop of Lorentzian resonances with linewidth of 2.5 ppm spaced by 2 ppm. Insets show the Gaussian fits of the Lorentzian resonances.

B Supporting Information

Supporting Information contains ^{23}Na NMR measurements at various MAS, estimates of spin-spin relaxation times, ^{23}Na σ_{CG} as a function of Larmor frequency, and deconvolution data of the ^{19}F NMR spectra.

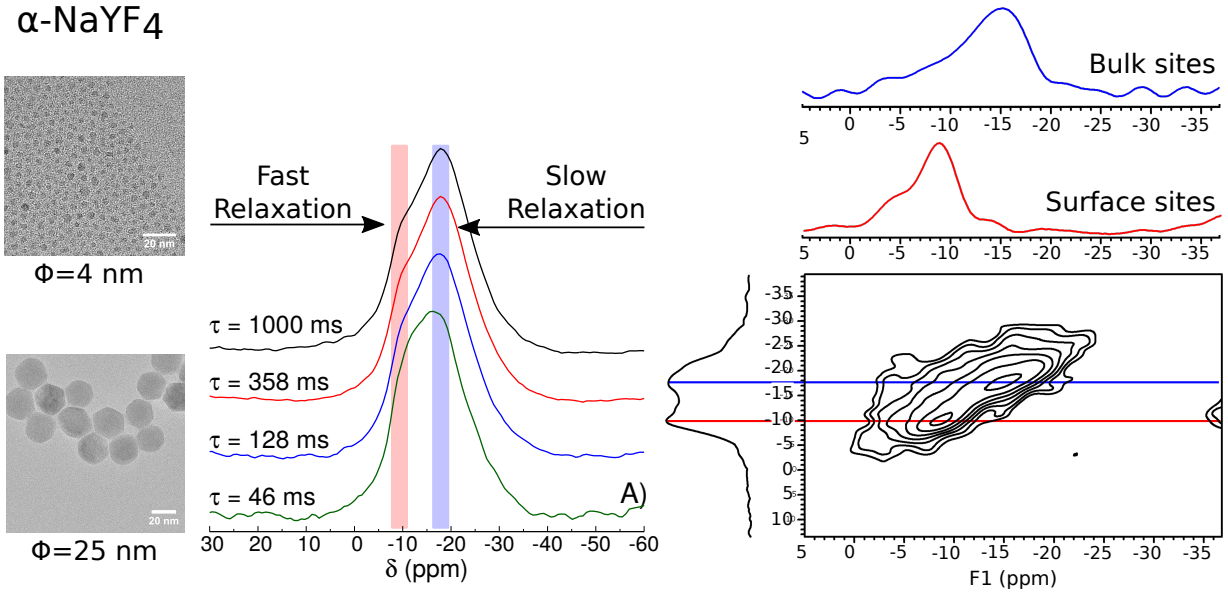

TOC Graphic.

Acknowledgement

Authors acknowledge the Brazilian funding agencies São Paulo Research Foundation (FAPESP) and National Council for Scientific and Technological Development (CNPq) for the supports UFABC Tematico 2011/19924-2, UNICAMP Tematico 2012/04870-7, FAPESP 2016/15780-0, FAPESP 2016/14436-3, Fapesp 2018/21025-5, and CNPq Universal Project 404951/2016-3. TEM was performed at LNNano, Centro Nacional de Pesquisa em Energia e Materiais (CNPEM) in Campinas, SP, Brazil. RRU acknowledges JP FAPESP 2012/05903-6 and CNPq 307668/2015-0. Additional images of electron microscopy were obtained by a collaboration with INCT/INOMAT (National Institute for Complex Functional Materials financed by grant 2014/50906-9, FAPESP). The authors are grateful to the Multiuser Central Facilities (UFABC) for the experimental support. Special thanks go to Dr. Antoine Champetier de Ribes from University of California, Davis, for proofreading the article, and Prof. Hellmut Eckert and Prof. José Schneider from the Physics Institute of São Carlos, University of São Paulo (IFSC/USP), for making available the NMR facilities and for valuable discussions and

suggestions.

References

(1) Sun, C.-J.; Xu, Z.; Hu, B.; Yi, G. S.; Chow, G. M.; Shen, J. Application of NaYF4:Yb, Er upconversion fluorescence nanocrystals for solution-processed near infrared photodetectors. *Applied Physics Letters* **2007**, *91*, 191113.

(2) Chen, X.; Zhao, Z.; Jiang, M.; Que, D.; Shi, S.; Zheng, N. Preparation and photodynamic therapy application of NaYF4:Yb, Tm-NaYF4:Yb, Er multifunctional upconverting nanoparticles. *New J. Chem.* **2013**, *37*, 1782–1788.

(3) Cui, X.; Mathe, D.; Kovács, N.; Horváth, I.; Jauregui-Osoro, M.; Torres Martin de Rosales, R.; Mullen, G. E. D.; Wong, W.; Yan, Y.; Krüger, D. et al. Synthesis, Characterization, and Application of Core-Shell Co0.16Fe2.84O4NaYF4(Yb, Er) and Fe3O4NaYF4(Yb, Tm) Nanoparticle as Trimodal (MRI, PET/SPECT, and Optical) Imaging Agents. *Bioconjugate Chemistry* **2016**, *27*, 319–328, PMID: 26172432.

(4) Aebischer, A.; Hostettler, M.; Hauser, J.; Krämer, K.; Weber, T.; Güdel, H. U.; Bürgi, H.-B. Structural and Spectroscopic Characterization of Active Sites in a Family of Light-Emitting Sodium Lanthanide Tetrafluorides. *Angewandte Chemie International Edition* **2006**, *45*, 2802–2806.

(5) Zhou, B.; Shi, B.; Jin, D.; Liu, X. Controlling upconversion nanocrystals for emerging applications. *Nature Nanotechnology* **2015**, *10*, 924 EP, Review Article.

(6) Mai, H.-X.; Zhang, Y.-W.; Si, R.; Yan, Z.-G.; Sun, L.-d.; You, L.-P.; Yan, C.-H. High-Quality Sodium Rare-Earth Fluoride Nanocrystals: Controlled Synthesis and Optical Properties. *Journal of the American Chemical Society* **2006**, *128*, 6426–6436, PMID: 16683808.

(7) García-Flores, A. F.; Matias, J. S.; Garcia, D. J.; Martínez, E. D.; Cornaglia, P. S.; Lesseux, G. G.; Ribeiro, R. A.; Urbano, R. R.; Rettori, C. Crystal-field effects in Er^{3+}- and Yb^{3+}-doped hexagonal $NaYF_4$ nanoparticles. *Phys. Rev. B* **2017**, *96*, 165430.

(8) Hirsh, D. A.; Johnson, N. J. J.; van Veggel, F. C. J. M.; Schurko, R. W. Local Structure of Rare-Earth Fluorides in Bulk and Core/Shell Nanocrystalline Materials. *Chemistry of Materials* **2015**, *27*, 6495–6507.

(9) B. P. Sobolev, V. P. P., D. A. Mineev Low-temperature hexagonal modification of $NaYF_4$ having the gagarinite structure. *Dokl. Akad. Nauk SSSR* **1963**, *150*, 791–794.

(10) Roy, D. M.; Roy, R. Controlled Massively Defective Crystalline Solutions with the Fluorite Structure. *J. Electrochem. Soc.* **1964**, *111*, 421–429.

(11) Mathews, M.; Ambekar, B.; Tyagi, A.; Köhler, J. High temperature X-ray diffraction studies on sodium yttrium fluoride. *Journal of Alloys and Compounds* **2004**, *377*, 162–166.

(12) Arnold, A. A.; Terskikh, V.; Li, Q. Y.; Naccache, R.; Marcotte, I.; Capobianco, J. A. Structure of NaYF4 Upconverting Nanoparticles: A Multinuclear Solid-State NMR and DFT Computational Study. *The Journal of Physical Chemistry C* **2013**, *117*, 25733–25741.

(13) Martin, M. N.; Newman, T.; Zhang, M.; Sun, L. D.; Yan, C. H.; Liu, G. Y.; Augustine, M. P. Using NMR Relaxometry to Probe Yb3+ - Er3+ Interactions in Highly Doped Nanocrystalline NaYF4 Nanostructures. *The Journal of Physical Chemistry C* **2019**, *123*, 10–16.

(14) Wang, F.; Deng, R.; Liu, X. Preparation of core-shell NaGdF4 nanoparticles doped with luminescent lanthanide ions to be used as upconversion-based probes. *Nature Protocols* **2014**, *9*, 1634 EP.

(15) Liu, J.; Chen, G.; Hao, S.; Yang, C. Sub-6 nm monodisperse hexagonal core/shell NaGdF4 nanocrystals with enhanced upconversion photoluminescence. *Nanoscale* **2017**, *9*, 91–98.

(16) Boyer, J.-C.; Cuccia, L. A.; Capobianco, J. A. Synthesis of Colloidal Upconverting NaYF4: Er3+/Yb3+ and Tm3+/Yb3+ Monodisperse Nanocrystals. *Nano Letters* **2007**, *7*, 847–852, PMID: 17302461.

(17) Schneider, C. A.; Rasband, W. S.; Eliceiri, K. W. NIH Image to ImageJ: 25 years of image analysis. *Nature Methods* **2012**, *9*, 671–675.

(18) Frydman, L.; Harwood, J. S. Isotropic Spectra of Half-Integer Quadrupolar Spins from Bidimensional Magic-Angle Spinning NMR. *Journal of the American Chemical Society* **1995**, *117*, 5367–5368.

(19) Medek, A.; Harwood, J. S.; Frydman, L. Multiple-Quantum Magic-Angle Spinning NMR: A New Method for the Study of Quadrupolar Nuclei in Solids. *Journal of the American Chemical Society* **1995**, *117*, 12779–12787.

(20) Brown, S. P.; Heyes, S. J.; Wimperis, S. Two-Dimensional MAS Multiple-Quantum NMR of Quadrupolar Nuclei. Removal of Inhomogeneous Second-Order Broadening. *Journal of Magnetic Resonance, Series A* **1996**, *119*, 280 – 284.

(21) Amoureux, J.-P.; Fernandez, C.; Steuernagel, S. ZFiltering in MQMAS NMR. *Journal of Magnetic Resonance, Series A* **1996**, *123*, 116 – 118.

(22) Koller, H.; Engelhardt, G.; Kentgens, A. P. M.; Sauer, J. 23Na NMR Spectroscopy of Solids: Interpretation of Quadrupole Interaction Parameters and Chemical Shifts. *The Journal of Physical Chemistry* **1994**, *98*, 1544–1551.

(23) Massiot, D.; Fayon, F.; Capron, M.; King, I.; Le Calvé, S.; Alonso, B.; Durand, J.-O.;

Bujoli, B.; Gan, Z.; Hoatson, G. Modelling one- and two-dimensional solid-state NMR spectra. *Magnetic Resonance in Chemistry 40*, 70–76.

(24) Bennett, A. E.; Rienstra, C. M.; Auger, M.; Lakshmi, K. V.; Griffin, R. G. Heteronuclear decoupling in rotating solids. *The Journal of Chemical Physics* **1995**, *103*, 6951–6958.

(25) Zheng, A.; Liu, S.-B.; Deng, F. 19F Chemical Shift of Crystalline Metal Fluorides: Theoretical Predictions Based on Periodic Structure Models. *The Journal of Physical Chemistry C* **2009**, *113*, 15018–15023.

(26) Hargreaves, J. S. J. Some considerations related to the use of the Scherrer equation in powder X-ray diffraction as applied to heterogeneous catalysts. *Catalysis, Structure & Reactivity* **2016**, *2*, 33–37.

(27) *See supporting information at http://dx.doi.org/address for ^{23}Na NMR measurements at various MAS, estimates of spin-spin relaxation times, ^{23}Na σ_{CG} as a function of Larmor frequency, and deconvolution data of the ^{19}F NMR spectra.*

(28) Kwak, H.-T.; Srinivasan, P.; Quine, J.; Massiot, D.; Gan, Z. Satellite transition rotational resonance of homonuclear quadrupolar spins: magic-angle effect on spin-echo decay and inversion recovery. *Chemical Physics Letters* **2003**, *376*, 75 – 82.

(29) Makrinich, M.; Gupta, R.; Polenova, T.; Goldbourt, A. Saturation capability of short phase modulated pulses facilitates the measurement of longitudinal relaxation times of quadrupolar nuclei. *Solid State Nuclear Magnetic Resonance* **2017**, *84*, 196 – 203, Solid-state NMR spectroscopy of Quadrupolar Nuclei.

(30) Andrew, E. R.; Tunstall, D. P. Spin-Lattice Relaxation in Imperfect Cubic Crystals and in Non-cubic Crystals. *Proceedings of the Physical Society* **1961**, *78*, 1.

(31) Hubbard, P. S. Nonexponential Nuclear Magnetic Relaxation by Quadrupole Interactions. *The Journal of Chemical Physics* **1970**, *53*, 985–987.

(32) Woessner, D.; Timken, H. The influence of MAS on spin-lattice relaxation curves and nuclear spin excitation of half-integer spin quadrupolar nuclei in solids. *Journal of Magnetic Resonance (1969)* **1990**, *90*, 411 – 419.

(33) V. M. Mikushev, E. V. C., A. M. Ulyashev; Chandoul, A. Controlled Massively Defective Crystalline Solutions with the Fluorite Structure. *Phys. Solid State* **2002**, *44*, 1044–1049.

(34) Yesinowski, J. P. Finding the true spinâĂŞlattice relaxation time for half-integral nuclei with non-zero quadrupole couplings. *Journal of Magnetic Resonance* **2015**, *252*, 135 – 144.

(35) Suter, A.; Mali, M.; Roos, J.; Brinkmann, D. *Journal of Physics: Condensed Matter* **1998**, *10*, 5977–5994.

(36) Apperley, D. C.; Markwell, A. F.; Frantsuzov, I.; Ilott, A. J.; Harris, R. K.; Hodgkinson, P. NMR characterisation of dynamics in solvates and desolvates of formoterol fumarate. *Phys. Chem. Chem. Phys.* **2013**, *15*, 6422–6430.

(37) Gordon, M. I.; Hoch, M. J. R. Quadrupolar spin-lattice relaxation in solids. *Journal of Physics C: Solid State Physics* **1978**, *11*, 783–795.

(38) Noriaki Okubo, M. I.; Yoshizak, R. Relaxation of 27Al NMR in Aluminium Tribromide due to Raman Process. *Z. Naturforsch.* **1996**, *51 a*, 277–282.

(39) Mutsuo Igarashi, S. H. R. Y., Noriaki Okubo; Cha, D. J. 23Na Spin-Lattice Relaxation Measurements in Dehydrated Na-X Zeolite. *Z. Naturforsch.* **1996**, *51 a*, 657–661.

(40) Yesinowski, J. P. Magnetization-recovery experiments for static and MAS-NMR of I=3/2 nuclei. *Journal of Magnetic Resonance* **2006**, *180*, 147 – 161.

(41) Bonera, G.; Borsa, F.; Rigamonti, A. Nuclear Quadrupole Spin-Lattice Relaxation and Critical Dynamics of Ferroelectric Crystals. *Phys. Rev. B* **1970**, *2*, 2784–2795.

(42) Jung, J.; Han, O.; Choh, S. Temperature dependence of 23Na NMR quadrupole parameters and spin-lattice relaxation rate in NaNO2 powder. *Solid State Communications* **1999**, *110*, 547 – 552.

(43) Weber, M. Nuclear quadrupole spin-lattice relaxation in solids. *Journal of Physics and Chemistry of Solids* **1961**, *17*, 267 – 277.

(44) Haase, J.; Pfeifer, H.; Oehme, W.; Klinowski, J. Longitudinal NMR relaxation of 27Al nuclei in zeolites. *Chemical Physics Letters* **1988**, *150*, 189 – 193.

(45) Haase, J.; Park, K. D.; Guo, K.; Timken, H. K. C.; Oldfield, E. Nuclear magnetic resonance spectroscopic study of spin-lattice relaxation of quadrupolar nuclei in zeolites. *The Journal of Physical Chemistry* **1991**, *95*, 6996–7002.

(46) Zhou, J.; Wen, S.; Liao, J.; Clarke, C.; Tawfik, S. A.; Ren, W.; Mi, C.; Wang, F.; Jin, D. Activation of the surface dark-layer to enhance upconversion in a thermal field. *Nature Photonics* **2018**, *12*, 154–158.

(47) Massiot, D.; Touzo, B.; Trumeau, D.; Coutures, J.; Virlet, J.; Florian, P.; Grandinetti, P. Two-dimensional magic-angle spinning isotropic reconstruction sequences for quadrupolar nuclei. *Solid State Nuclear Magnetic Resonance* **1996**, *6*, 73 – 83.

(48) Amoureux, J.-P.; Huguenard, C.; Engelke, F.; Taulelle, F. Unified representation of MQMAS and STMAS NMR of half-integer quadrupolar nuclei. *Chemical Physics Letters* **2002**, *356*, 497 – 504.

(49) Slichter, C. P. *Principles of magnetic resonance*, 3rd ed.; Springer-Verlag Berlin ; New York, 1990; Chapter 10, pp x, 655 pages :.

(50) Ashbrook, S. E.; Duer, M. J. Structural information from quadrupolar nuclei in solid state NMR. *Concepts in Magnetic Resonance Part A* **2006**, *28A*, 183–248.

(51) Oshima, C.; Aizawa, T.; Souda, R.; Ishizawa, Y. Microscopic surface phonons of MgO(1 0 0) surface. *Solid State Communications* **1990**, *73*, 731 – 734.

(52) Lagos, M. J.; Trügler, A.; Hohenester, U.; Batson, P. E. Mapping vibrational surface and bulk modes in a single nanocube. *Nature* **2017**, *543*, 529 EP.

(53) Tien, C.; Charnaya, E. V.; Lee, M. K.; Baryshnikov, S. V.; Sun, S. Y.; Michel, D.; Böhlmann, W. Coexistence of melted and ferroelectric states in sodium nitrite within mesoporous sieves. *Phys. Rev. B* **2005**, *72*, 104105.

(54) Baryshnikov, S. V.; Tien, C.; Charnaya, E. V.; Lee, M. K.; Michel, D.; Böhlmann, W.; Stukova, E. V. Dielectric Properties of Mesoporous Sieves Filled with NaNO2. *Ferroelectrics* **2008**, *363*, 177–186.

(55) Thayer, A. M.; Steigerwald, M. L.; Duncan, T. M.; Douglass, D. C. NMR Study of Semiconductor Molecular Clusters. *Phys. Rev. Lett.* **1988**, *60*, 2673–2676.

(56) Lianos, P.; Thomas, J. Cadmium sulfide of small dimensions produced in inverted micelles. *Chemical Physics Letters* **1986**, *125*, 299 – 302.

(57) Kortan, A. R.; Hull, R.; Opila, R. L.; Bawendi, M. G.; Steigerwald, M. L.; Carroll, P. J.; Brus, L. E. Nucleation and Growth of CdSe on ZnS Quantum Crystallite Seeds, and Vice Versa, in Inverse Micelle Media. *Journal of the American Chemical Society* **1990**, *112*, 1327–1332.

(58) Lo, A. Y. H.; Sudarsan, V.; Sivakumar, S.; van Veggel, F.; Schurko, R. W. Multinuclear Solid-State NMR Spectroscopy of Doped Lanthanum Fluoride Nanoparticles. *Journal of the American Chemical Society* **2007**, *129*, 4687–4700, PMID: 17385858.

(59) Bessada, C.; Rakhmatullin, A.; Rollet, A.-L.; Zanghi, D. High temperature NMR approach of mixtures of rare earth and alkali fluorides: An insight into the local structure. *Journal of Fluorine Chemistry* **2009**, *130*, 45–52, Fluorine & Nuclear Energy.

(60) Wang, F.; Grey, C. P. Probing the Mechanism of Fluoride-Ion Conduction in LaF3 and Strontium-Doped LaF3 with High-Resolution 19F MAS NMR. *Chemistry of Materials* **1997**, *9*, 1068–1070.

(61) Ramana Reddy, M. V.; Narasimha Reddy, K. Characterization and electrical behaviour of NaYF4thin films. *physica status solidi (a)* **1986**, *95*, K193–K197.

(62) Shareefuddin, M.; Jamal, M.; Chary, M. N. Solid state battery with pure and doped sodium yttrium fluoride as the solid electrolyte. *Journal of Physics D: Applied Physics* **1995**, *28*, 440–442.

(63) Patro, L.; Hariharan, K. Fast fluoride ion conducting materials in solid state ionics: An overview. *Solid State Ionics* **2013**, *239*, 41 – 49.

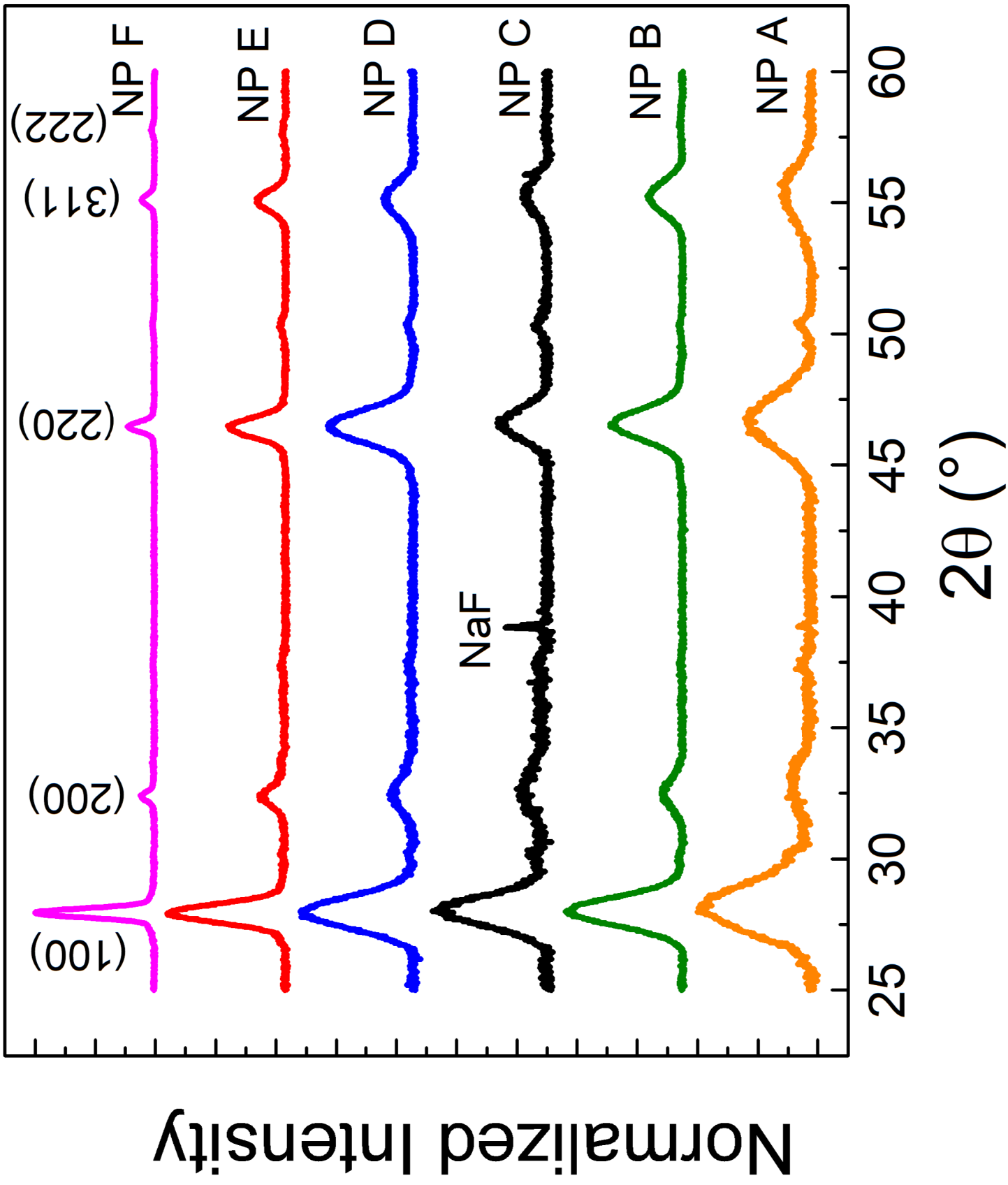
NP F
NP E
NP D
NP C
NP B
NP A
(222)
(311)
(220)
(200)
(100)
NaF
25
30
35
40
45
50
55
60
2θ (°)
Normalized Intensity

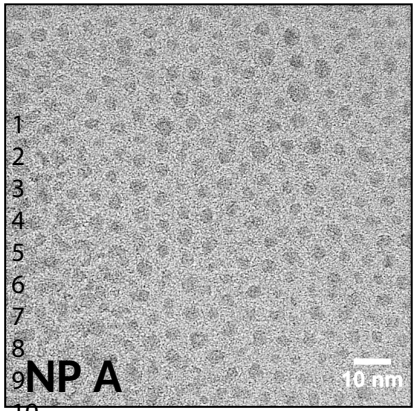
NP A
10 nm

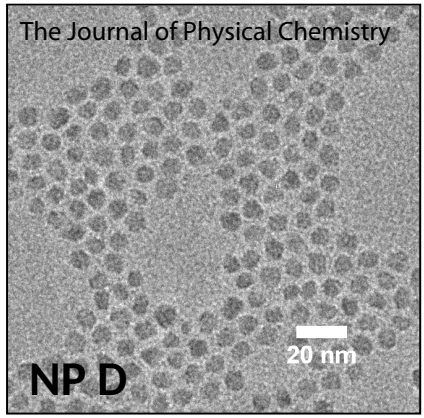
NP D
20 nm

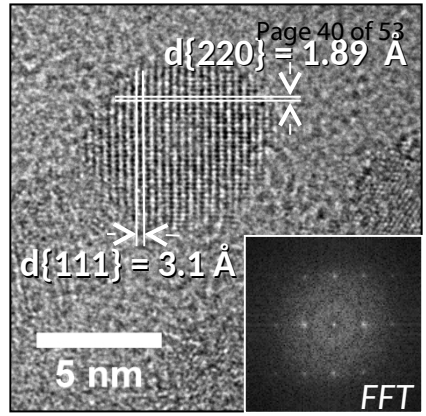
d{220} = 1.89 Å
d{111} = 3.1 Å
5 nm
FFT

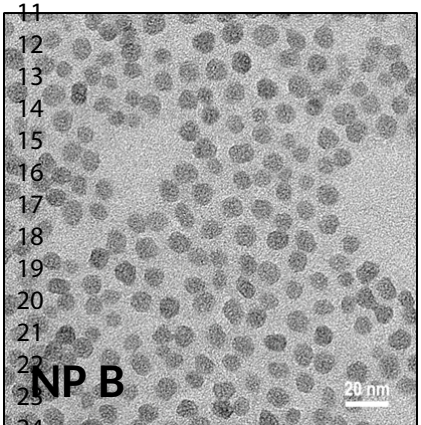
NP B
20 nm

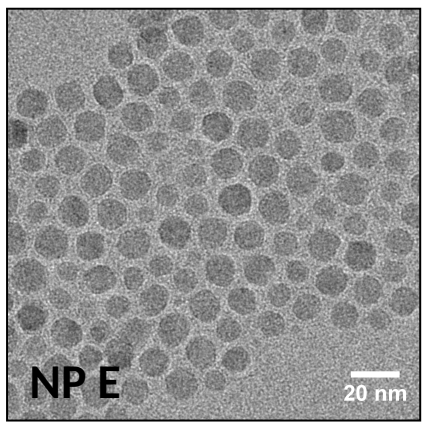
NP E
20 nm

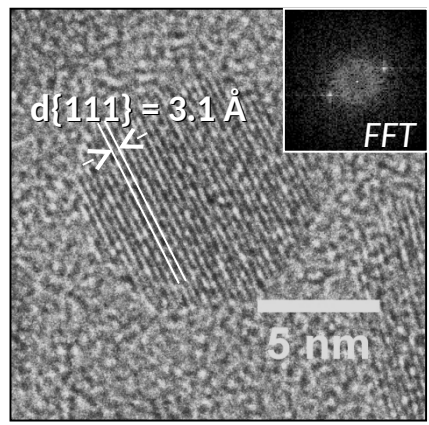
d{111} = 3.1 Å
FFT
5 nm

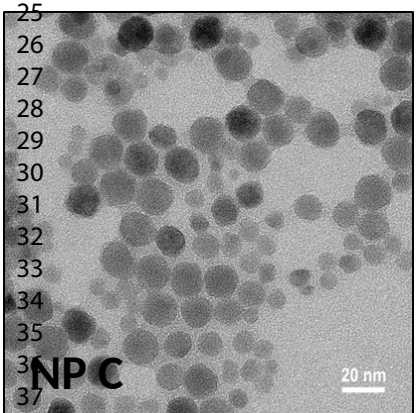
NP C
20 nm

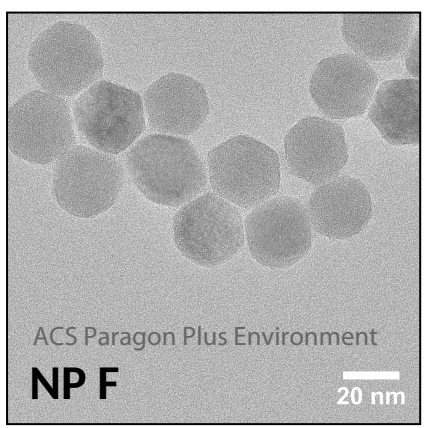
ACS Paragon Plus Environment
NP F
20 nm

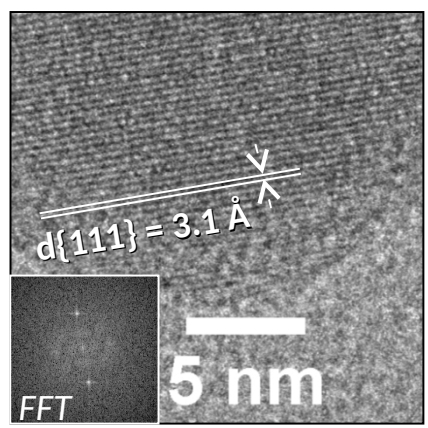
d{111} = 3.1 Å
FFT
5 nm

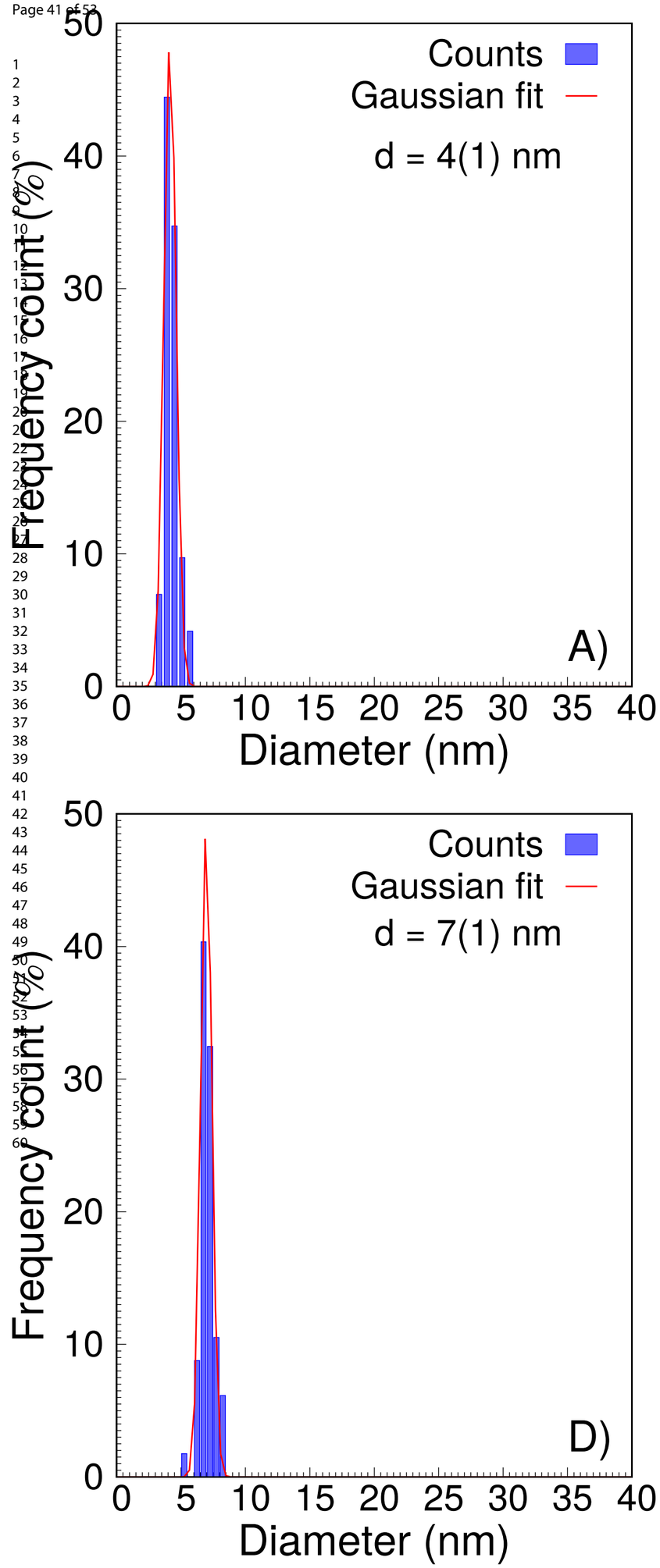
Counts
Gaussian fit
d = 4(1) nm
A)
Frequency count (%)
Diameter (nm)

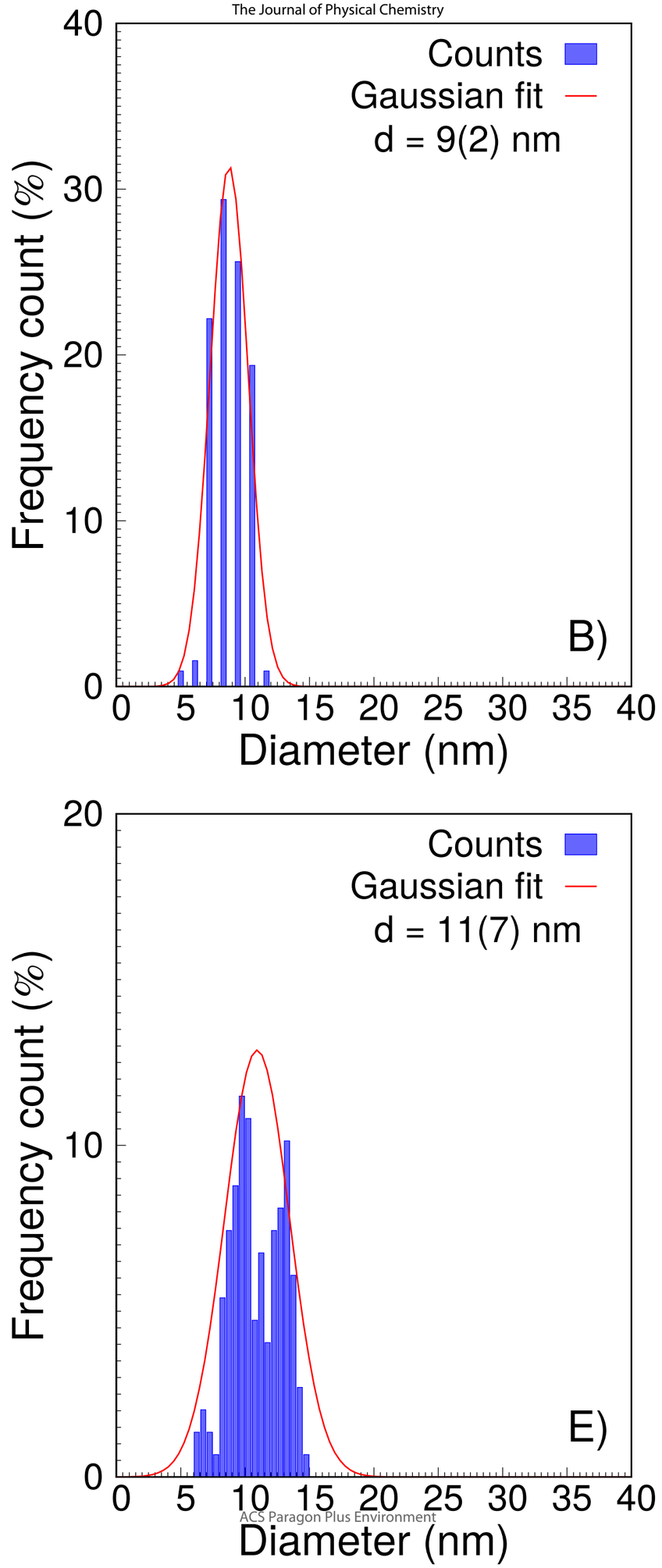
Counts
Gaussian fit
d = 9(2) nm
B)
Frequency count (%)
Diameter (nm)

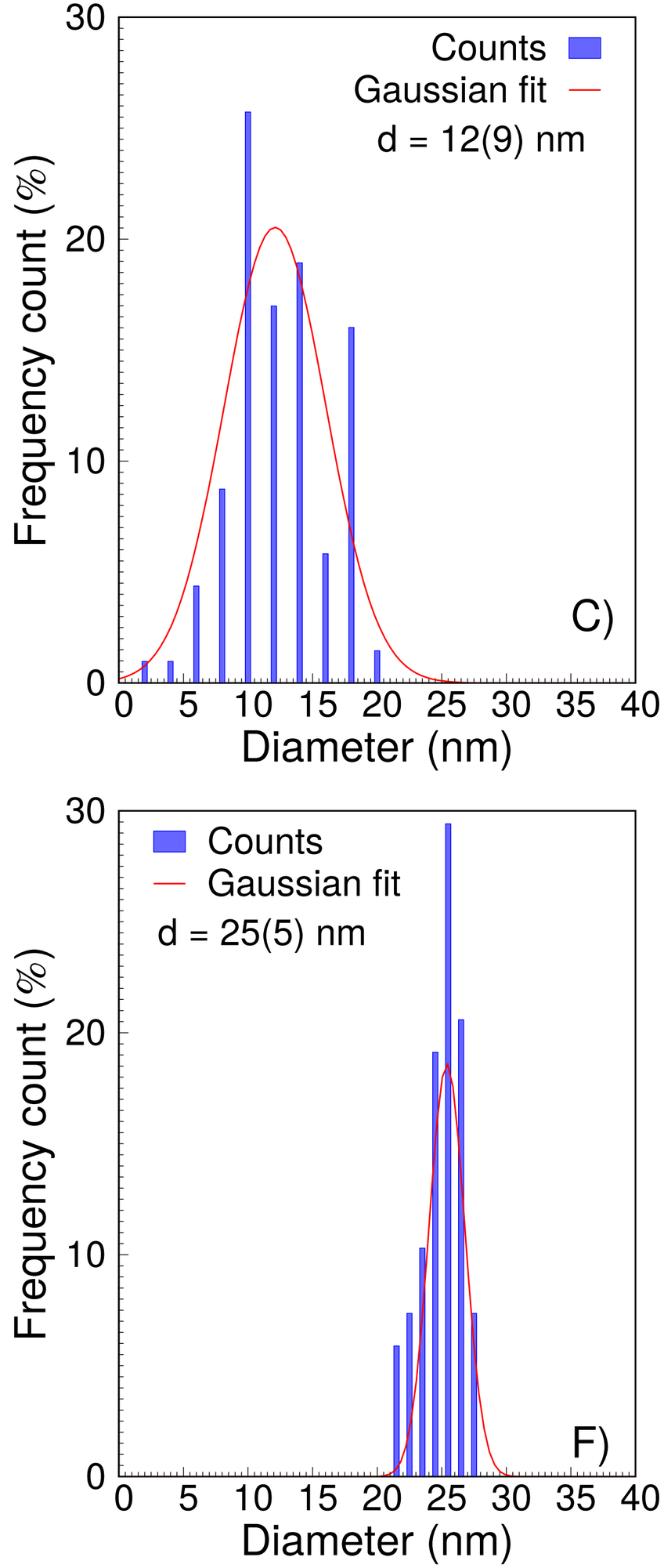
Counts
Gaussian fit
d = 12(9) nm
C)
Frequency count (%)
Diameter (nm)

Counts
Gaussian fit
d = 7(1) nm
D)
Frequency count (%)
Diameter (nm)

Counts
Gaussian fit
d = 11(7) nm
E)
Frequency count (%)
Diameter (nm)

Counts
Gaussian fit
d = 25(5) nm
F)
Frequency count (%)
Diameter (nm)

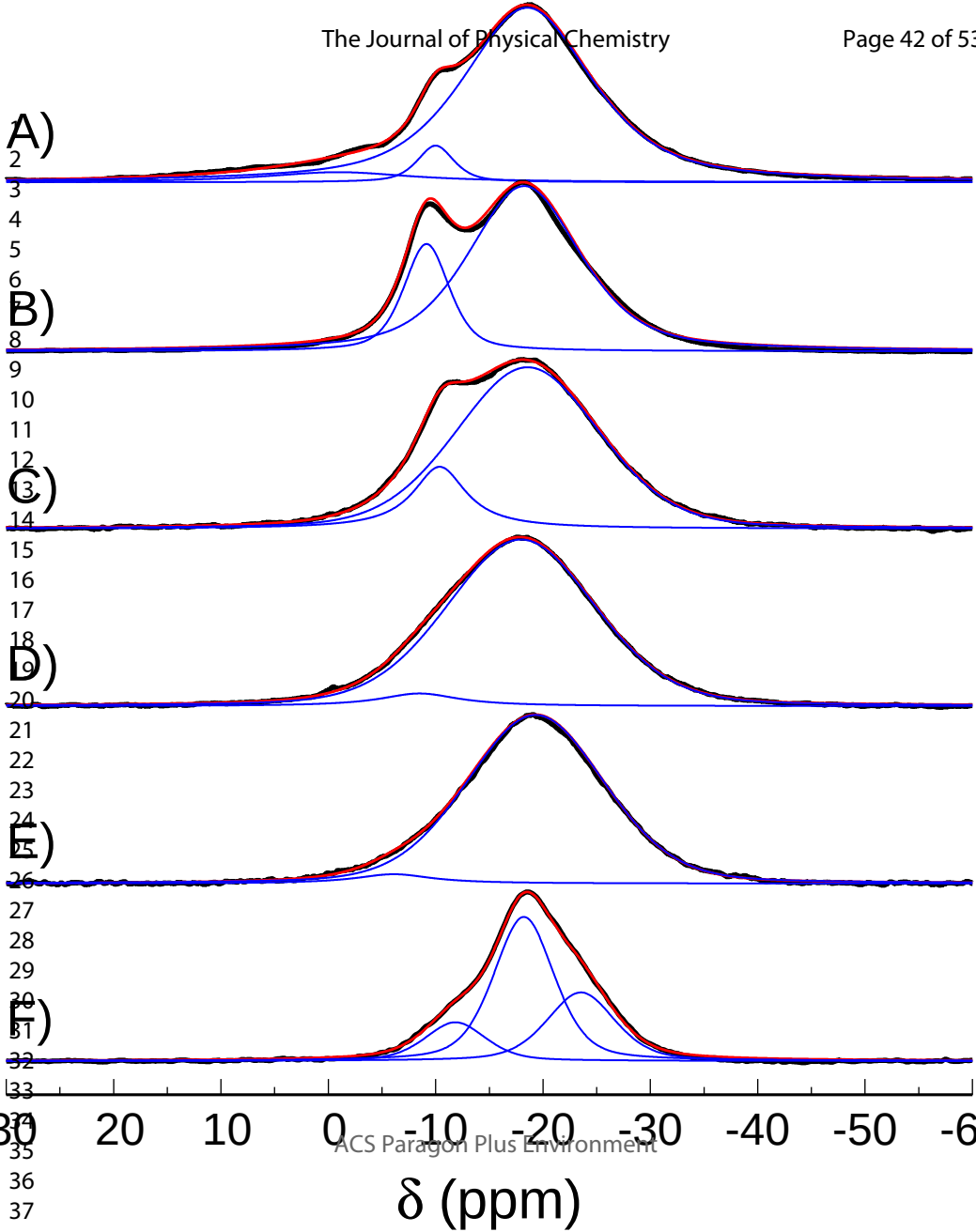

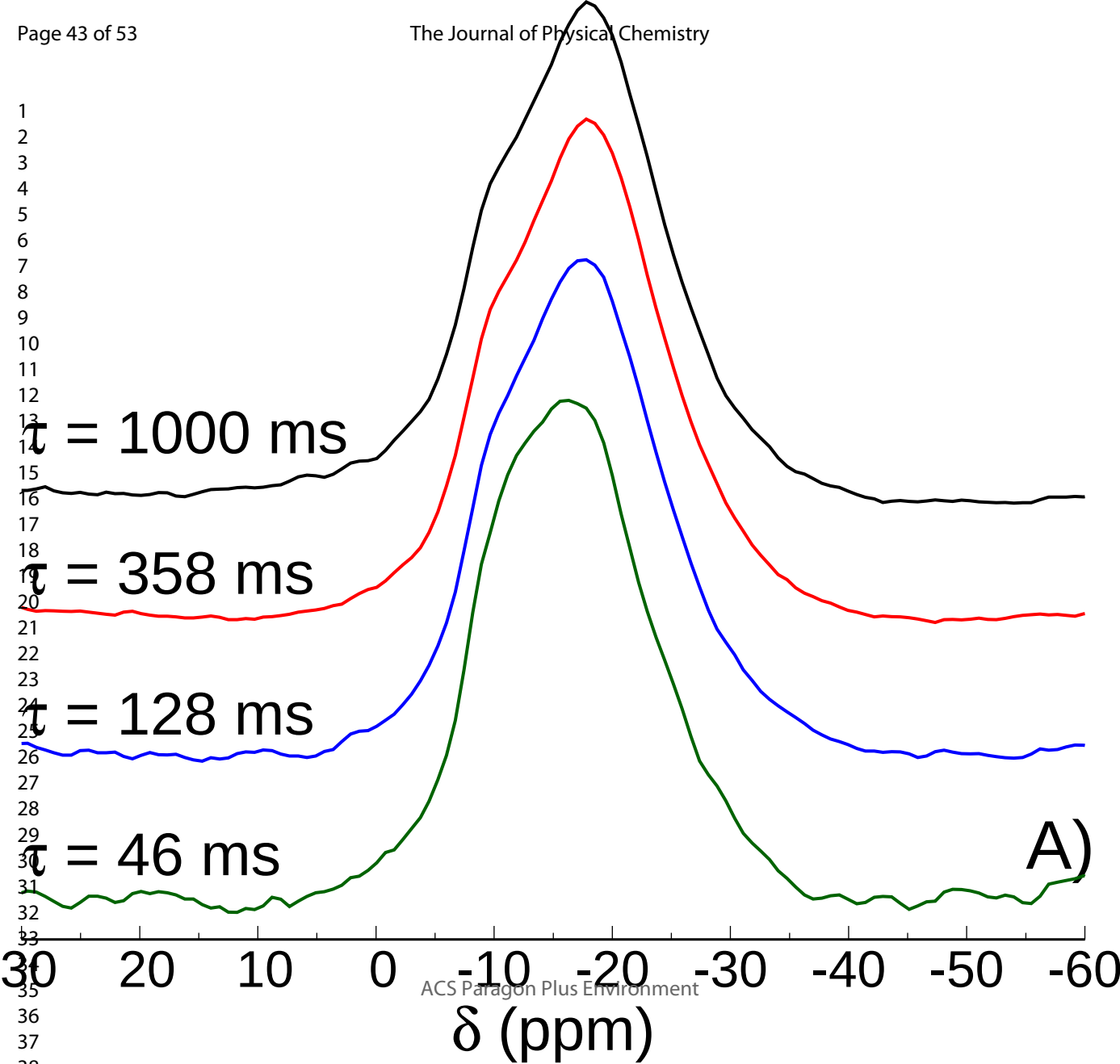

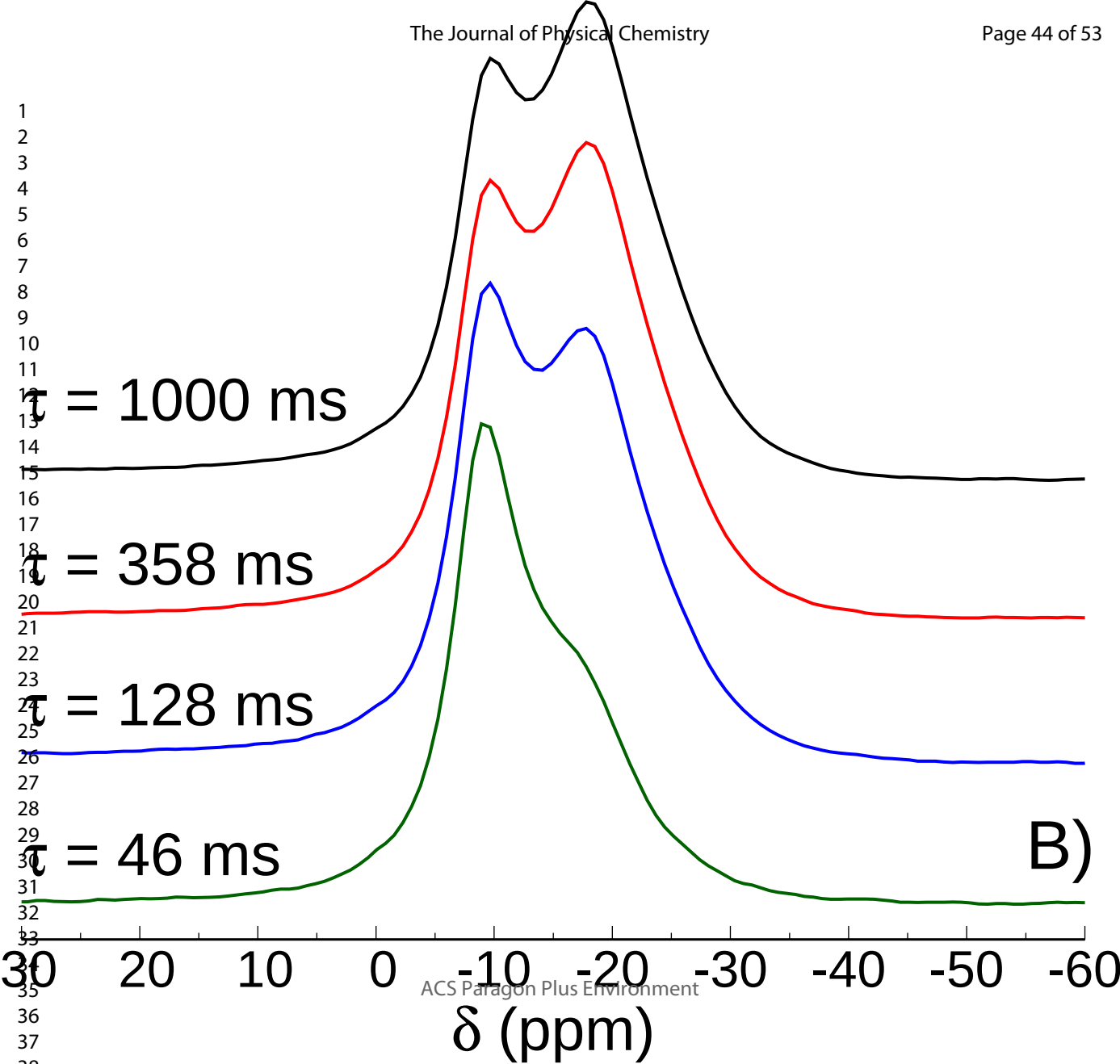

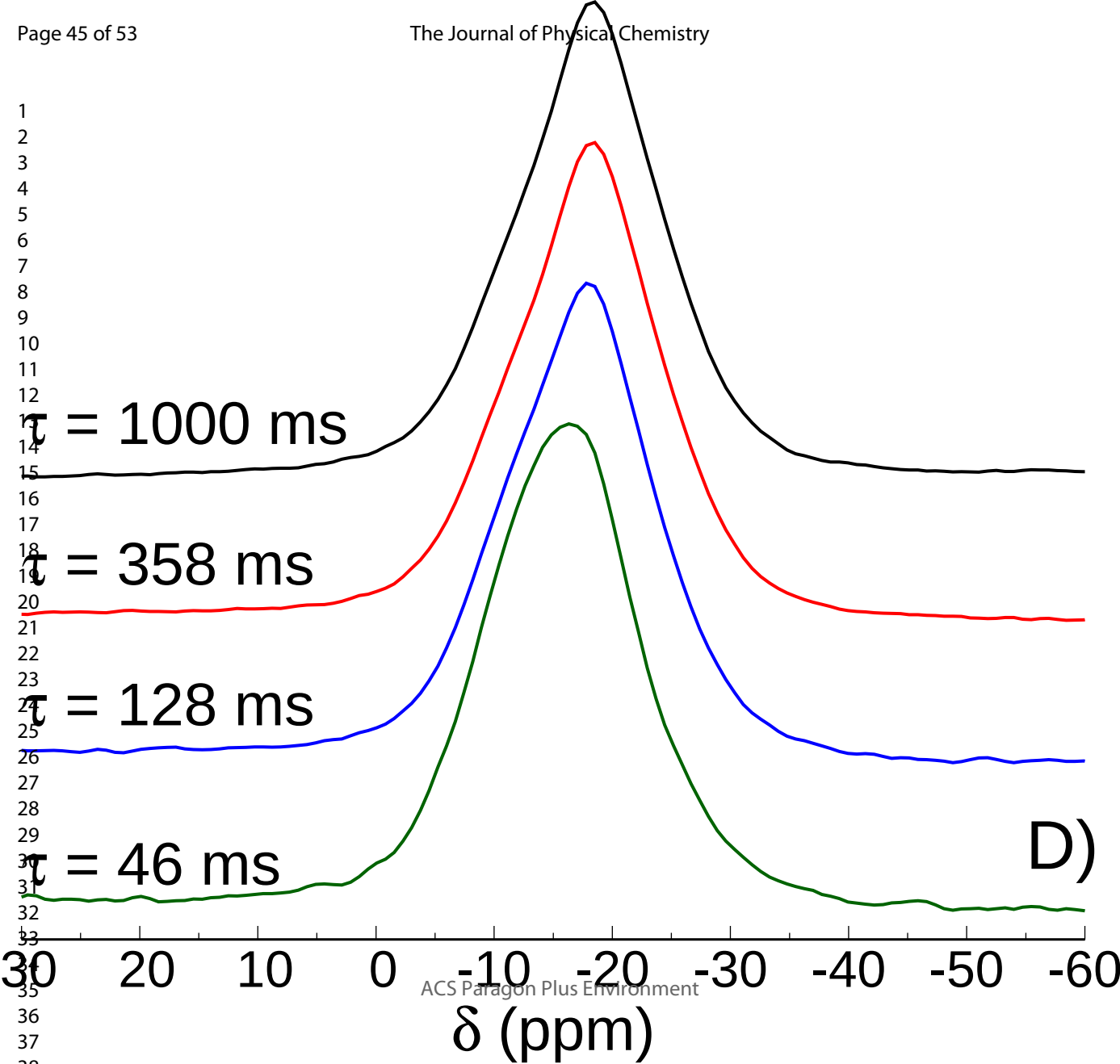

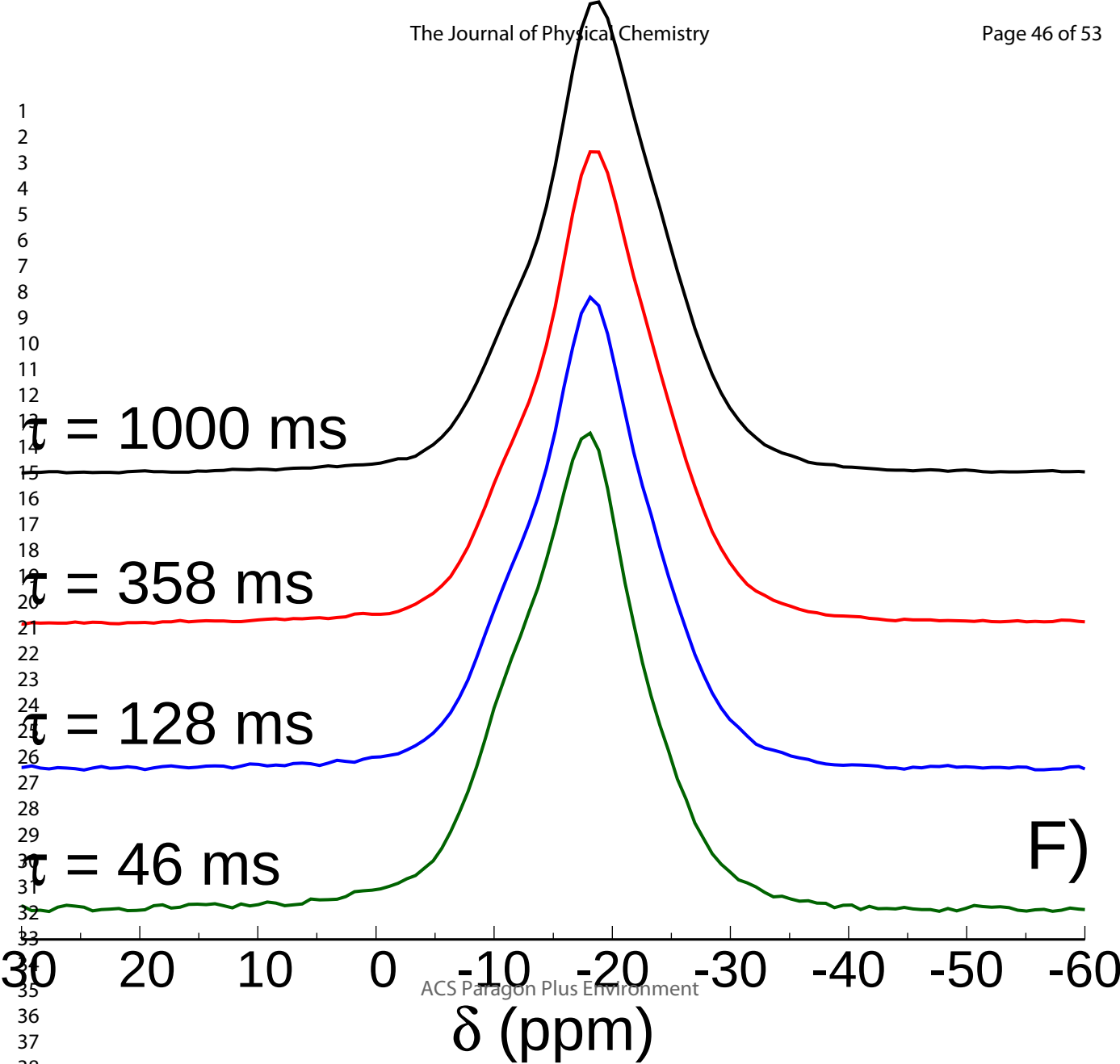

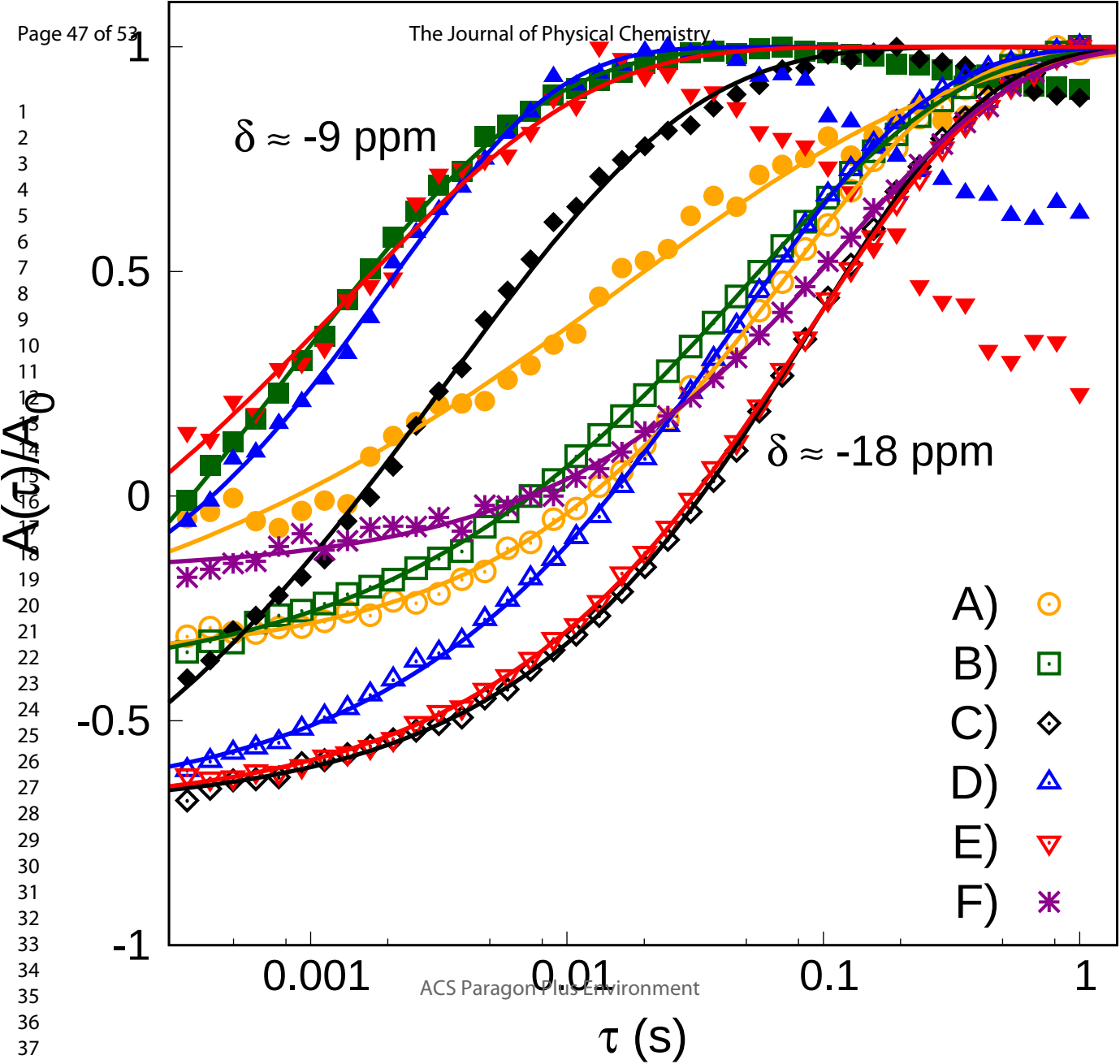
δ ≈ -9 ppm
δ ≈ -18 ppm
A)
B)
C)
D)
E)
F)
A(τ)/A0
τ (s)
1
0.5
0
-0.5
-1
0.001
0.01
0.1
1

A)
B)
D)
F)
-35
-30
-25
-20
-15
-10
-5
0
5
10
5 0 -5 -10 -15 -20 -25 -30 -35
F1 (ppm)
F2 (ppm)

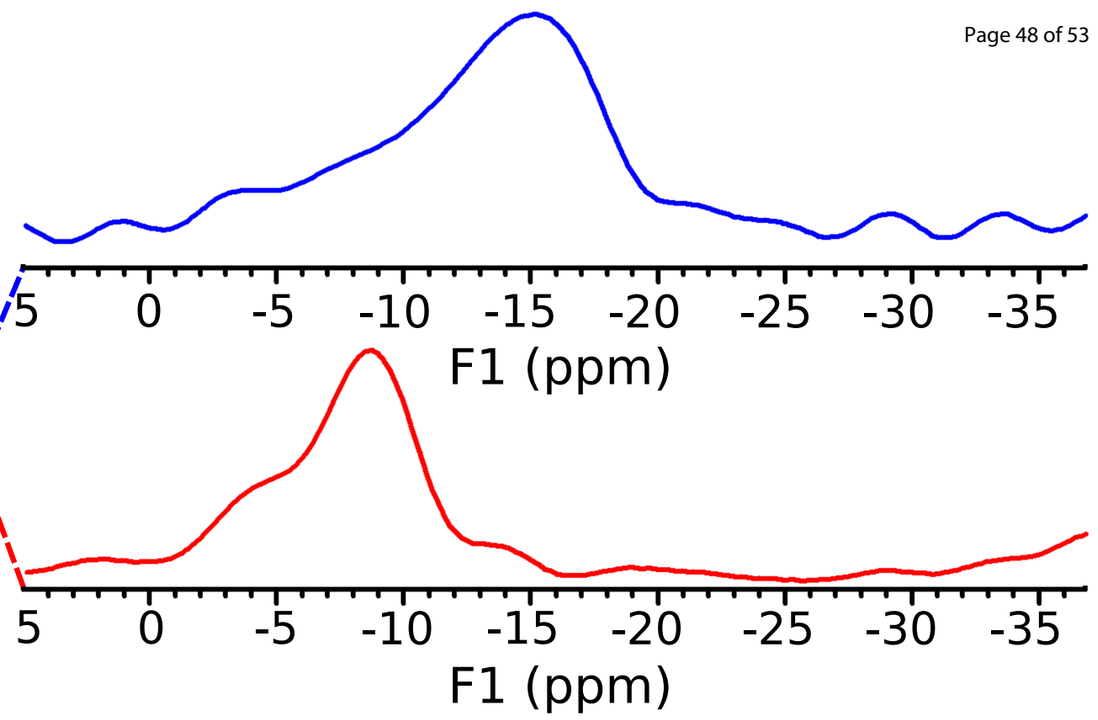
5 0 -5 -10 -15 -20 -25 -30 -35
F1 (ppm)

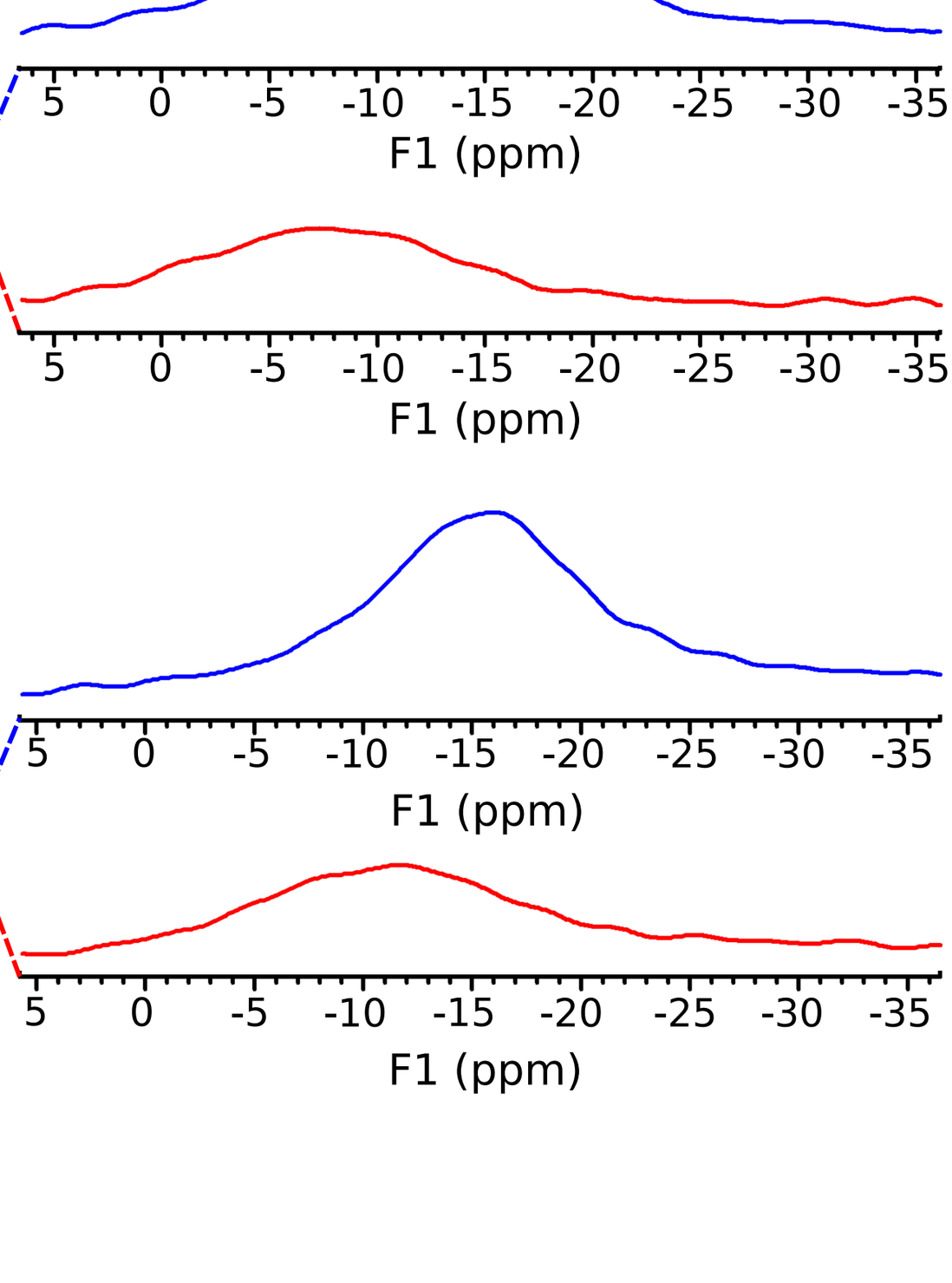
5 0 -5 -10 -15 -20 -25 -30 -35
F1 (ppm)

5 0 -5 -10 -15 -20 -25 -30 -35
F1 (ppm)

5 0 -5 -10 -15 -20 -25 -30 -35
F1 (ppm)

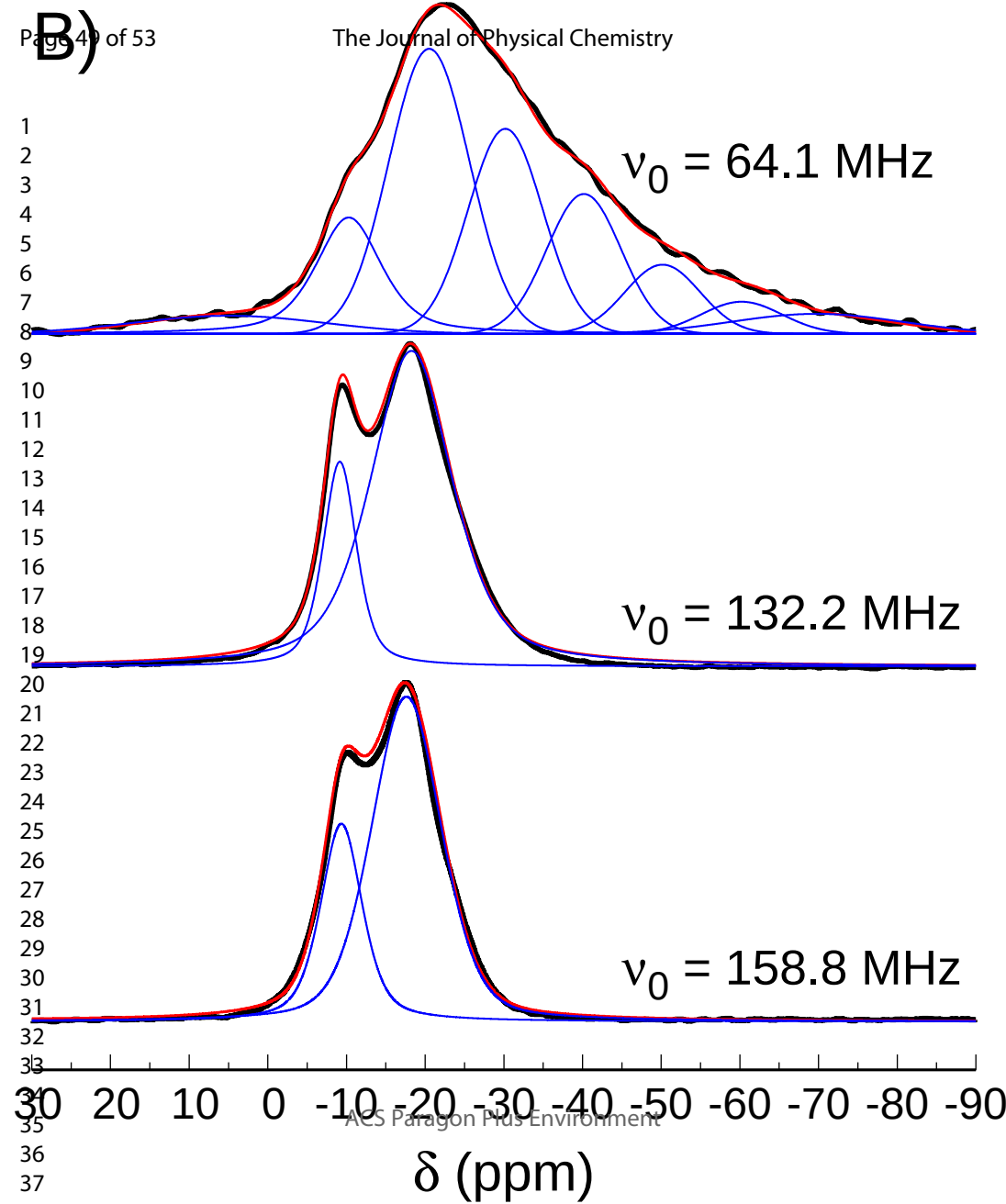

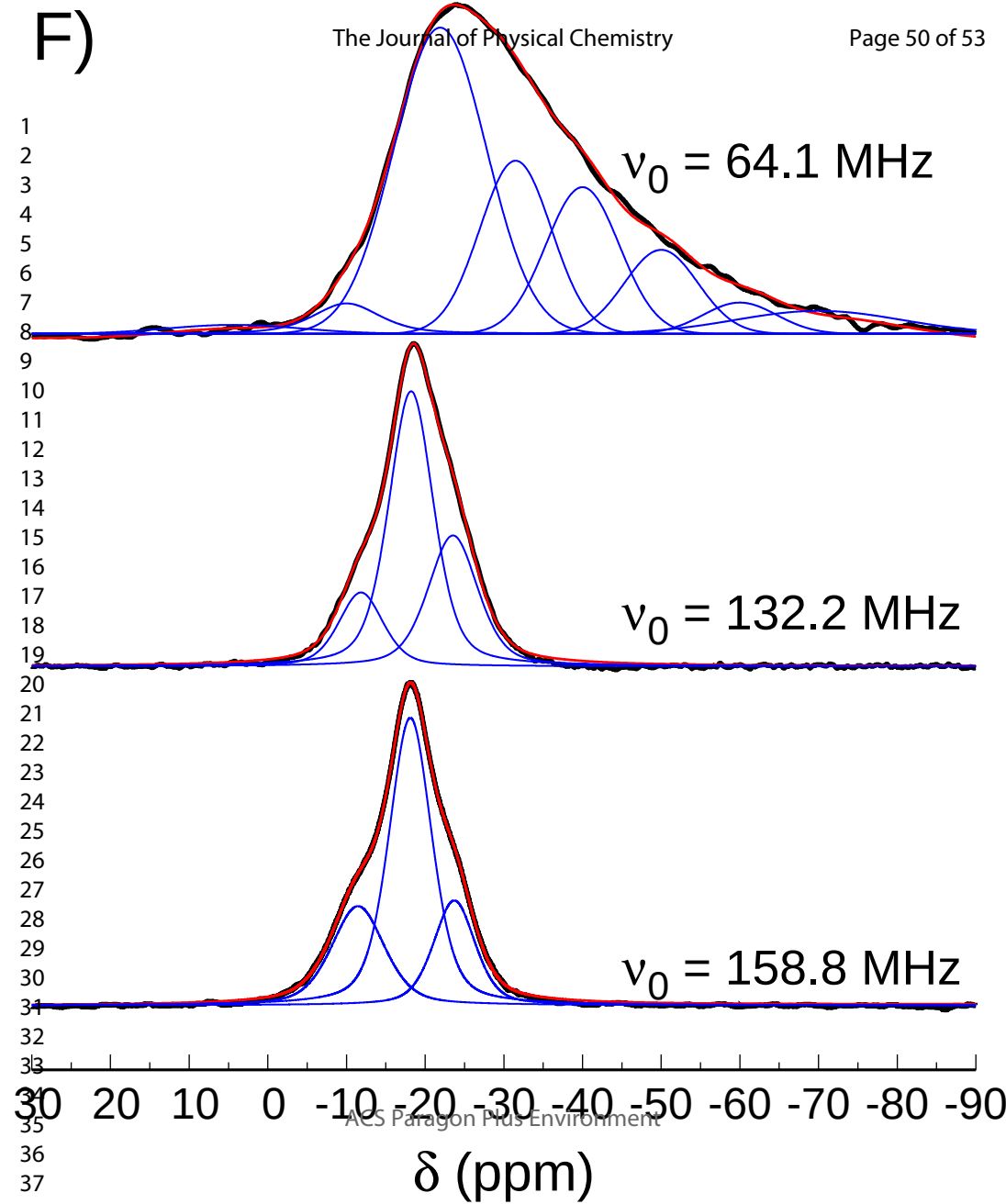

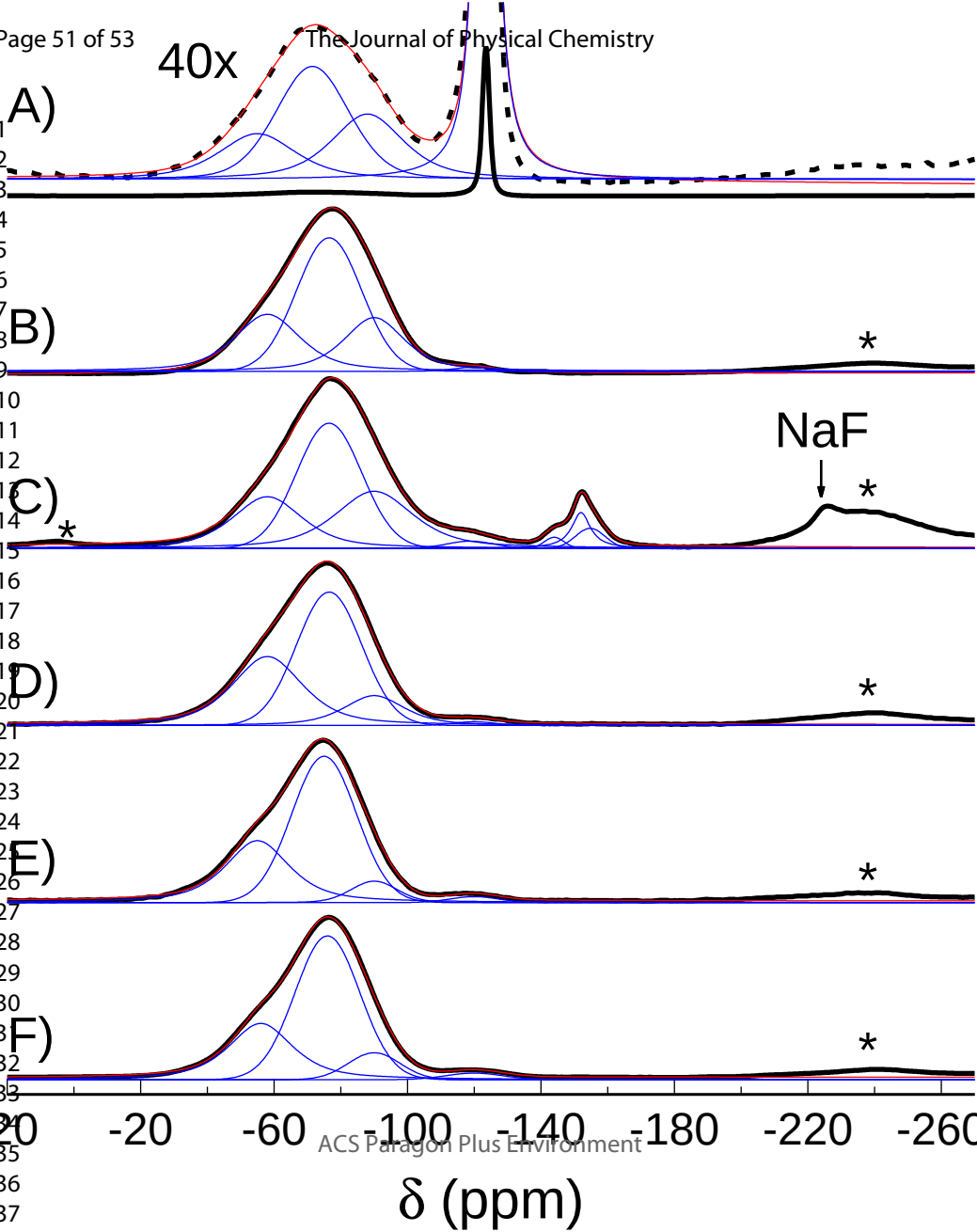

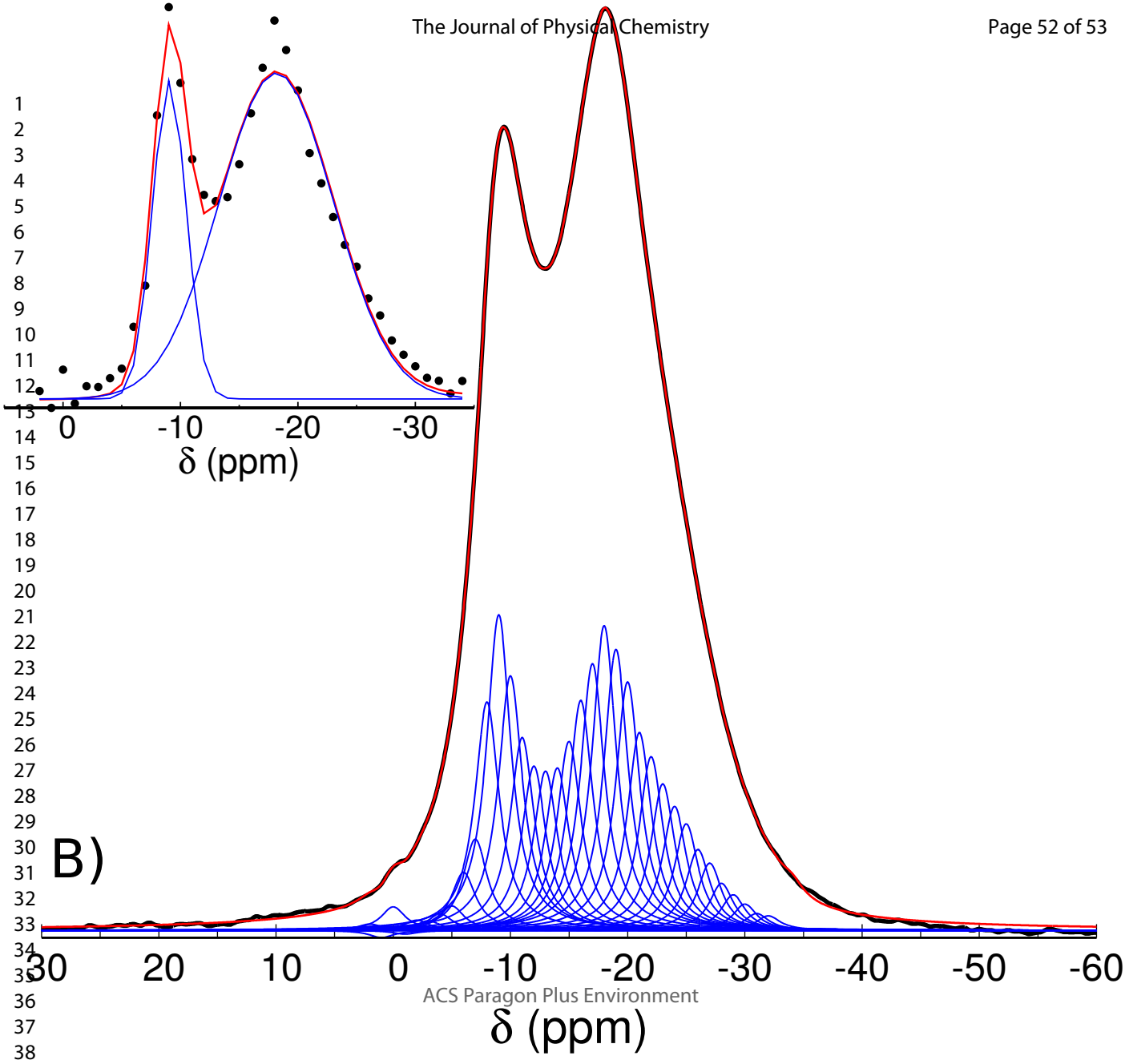
0
-10
-20
-30
δ (ppm)
B)
30
20
10
0
-10
-20
-30
-40
-50
-60
ACS Paragon Plus Environment
δ (ppm)

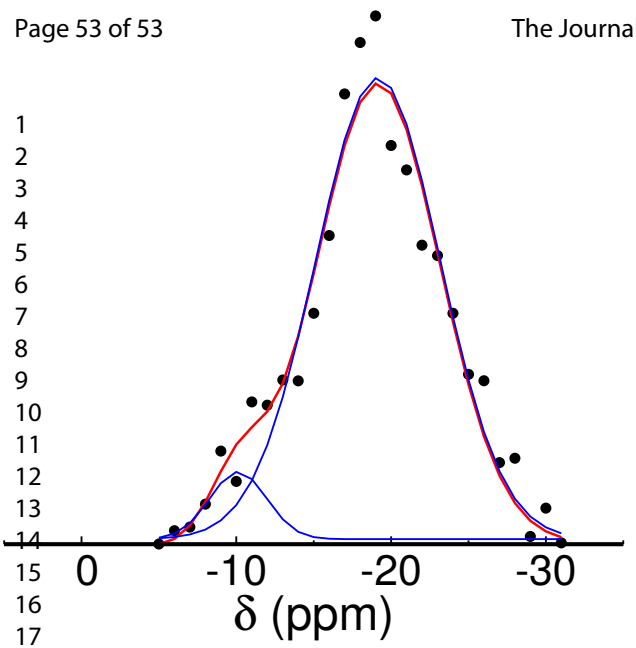

F)

30 20 10 0 -10 -20 -30 -40 -50 -60

δ (ppm)